

Regular and Chaotic Dynamics of Triaxial Stellar Systems

Monica Valluri and David Merritt

Department of Physics and Astronomy, Rutgers University, New Brunswick, NJ 08855.

Rutgers Astrophysics Preprint Series No. 214

ABSTRACT

We use Laskar’s frequency mapping technique to study the dynamics of triaxial galaxies with central density cusps and nuclear black holes. For ensembles of $\sim 10^4$ orbits, we numerically compute the three fundamental frequencies of the motion, allowing us to map out the Arnold web. We also compute diffusion rates of stochastic orbits in frequency space. The objects of greatest importance in structuring phase space are found to be the 3-dimensional resonant tori, regions where the fundamental frequencies satisfy a relation of the form $0 = l\omega_1 + m\omega_2 + n\omega_3$ with integer (l, m, n) . When stable, resonant tori generate phase space regions in which the motion is regular; these regions are not necessarily associated with a stable periodic orbit as in systems with only two degrees of freedom. Boxlike orbits are generically stochastic but some tube orbits are stochastic as well. The spectrum of diffusion rates for boxlike orbits at a given energy is well approximated as a power law over at least six decades. Models with high central concentrations – steep central cusps or massive black holes – exhibit the most stochasticity. Even a modest black hole, with a mass $\sim 0.3\%$ the mass of the galaxy, is as effective as the steepest central density cusp at inducing stochastic diffusion. There is a transition to global stochasticity in boxlike phase space when the mass of a central black hole exceeds $\sim 2\%$ of the galaxy mass. We estimate the dependence of orbital evolution rates on galaxy structural parameters. We predict a greater average degree of dynamical evolution in faint elliptical galaxies due to their high central densities and short crossing times. The evolution time is estimated to be shorter than a galaxy lifetime for absolute magnitudes fainter than about -19 or -20 , consistent with the observed change in many elliptical galaxy properties at this luminosity.

1 INTRODUCTION

Motion in a smooth gravitational field becomes quite simple if the number of isolating integrals equals or exceeds the number of degrees of freedom, and much work in galactic dynamics has focussed on finding integrable or near-integrable models for galactic potentials. Kuzmin (1956, 1973) showed that there is a unique, ellipsoidally-stratified mass model for which the corresponding potential has three global integrals of the motion, quadratic in the velocities. Kuzmin’s model – explored in detail by de Zeeuw (1985) who christened it the “Perfect Ellipsoid” – has a large, constant-density core in which the orbital motion is that of a 3-D harmonic oscillator. Every orbit in the core of the Perfect Ellipsoid fills a rectangular parallelepiped, or box. At higher energies in the Perfect Ellipsoid, box orbits persist and three new orbit families appear: the tubes, orbits that preserve the direction of their circulation around either the long or short axis of the figure. Tube orbits respect an integral of the motion analogous to the angular momentum, and hence – unlike box orbits – avoid the center. All integrable triaxial potentials have a similar orbital structure (Hunter 1995).

The large core of the Perfect Ellipsoid is a poor match to real elliptical galaxies, all of which exhibit power-law cusps in the stellar density at small radii (Ferrarese et al. 1994; Merritt & Fridman 1995; Gebhardt et al. 1996). There is increasingly strong evidence that many elliptical galaxies and bulges also contain massive central objects, possibly the black holes that are thought to have powered quasars (Kormendy & Richstone 1995). While the masses of these dark central components are often very uncertain, typical estimates are $10^{-3} \lesssim M_h/M_g \lesssim 10^{-2}$, where M_h is the black hole mass inferred from the orbital motions of surrounding stars and gas and M_g is the stellar mass of the host galaxy or (in the case of a spiral galaxy) the mass of the stellar bulge. Some galaxies, like M32, the dwarf companion to the nearby Andromeda galaxy, are known to contain both a steep stellar cusp ($\rho \propto r^{-1.6}$) and a dynamically-significant black hole ($M_h/M_g \sim 0.003$).

The purpose of the present study is to explore the orbital dynamics of realistic triaxial potentials in a systematic way. One goal is to understand how the structure of triaxial phase space differs from that of axisymmetric systems. Another is to estimate the rate at which chaos implies

changes in the structure of a triaxial galaxy, and to understand how this rate depends on galaxy properties. In a pioneering study, Goodman & Schwarzschild (1981) found that the boxlike orbits in a triaxial model with a smooth core were often stochastic, but that the behavior of these orbits was essentially regular for at least 50 oscillations. On the other hand, Merritt & Fridman (1996) found that the stochasticity in triaxial models with $\rho \propto r^{-2}$ density cusps produced significant changes in the appearance of boxlike orbits after just a few tens of oscillations. Merritt & Valluri (1996) went on to calculate timescales for mixing in these strongly chaotic potentials; they found that ensembles of stochastic trajectories could evolve toward invariant distributions – corresponding to an approximately uniform filling of stochastic phase space – on timescales of only $10^1 - 10^2$ orbital periods. Kandrup and coworkers (Kandrup & Mahon 1994; Mahon et al. 1995) noted similar, rapid rates of chaotic mixing in a variety of two-dimensional systems. Taken together, these results suggest that the characteristic time over which chaos manifests itself in the orbital motion of a triaxial galaxy is strongly dependent on its radial mass distribution. Presumably, this dependence reflects the sensitivity of boxlike orbits to deflections that occur during close passages to the galaxy center.

Here we use Laskar’s frequency mapping technique (§2) to look in much more detail at the structure of regular and chaotic phase space in realistic triaxial potentials. Laskar’s technique – summarized in more detail below – allows one to quickly and accurately compute the fundamental frequencies that characterize the quasi-periodic motion of regular orbits on their invariant tori. In addition, one can compute the rate at which these frequencies change as a stochastic orbit diffuses from one torus to another. The entire phase space at a given energy can then be represented on a single diagram, the frequency map, which shows the way in which an otherwise-integrable phase space is modified by the existence of resonances between the three degrees of freedom. The resonances that are most important for determining the structure of phase space can immediately be picked out.

The models considered in this study are the triaxial generalizations of the spherical models discussed by Dehnen (1993), Carollo (1993) and Tremaine *et al.* (1994). These models have a mass density

$$\rho(m) = \frac{(3 - \gamma)M}{4\pi abc} m^{-\gamma} (1 + m)^{-(4-\gamma)}, \quad 0 \leq \gamma < 3 \quad (1)$$

with

$$m^2 = \frac{x^2}{a^2} + \frac{y^2}{b^2} + \frac{z^2}{c^2}, \quad a \geq b \geq c \geq 0, \quad (2)$$

and M the total mass. The mass is stratified on ellipsoids with axis ratios $a : b : c$; the x [z] axis is the long [short] axis. The parameter γ determines the slope of the central density cusp. For $\gamma = 0$ the model has a finite-density core, while for all $\gamma > 0$ the central density is infinite. The strongest cusps that we will consider here have $\gamma = 2$, i.e. $\rho \propto m^{-2}$ at small radii. Henceforth we will refer to this model as a “ γ -model” or as “Dehnen’s model.” In the spherical case, the radial force in this model is

$$-\frac{\partial\Phi}{\partial r} = -\frac{GM}{a^2} \left(\frac{r}{a}\right)^{1-\gamma} \left(1 + \frac{r}{a}\right)^{\gamma-3}, \quad (3)$$

which is finite at the center for $\gamma < 1$ (“weak cusp”) and divergent for $\gamma \geq 1$ (“strong cusp”). To represent the effect on the stellar motions of a central black hole, we also consider models with an added central point of mass M_h . The γ -model is a reasonable description of the stellar density at small and intermediate radii in elliptical galaxies. Our choice of this model is motivated by the expectation that the central regions of a triaxial galaxy are the most important for determining the behavior of the boxlike orbits. One of our principal objectives will be to establish whether there is a critical value of cusp slope γ or black hole mass M_h at which a globally significant transition occurs in the structure of phase space.

We find (§3) that the motion of boxlike orbits in triaxial γ -models is generically chaotic, but that the timescale for diffusion in stochastic phase space exhibits great variation, both within a single model and as a function of γ and M_h . We confirm the result of Papaphilippou & Laskar (1998) that the objects of fundamental importance for structuring phase space are the 3-dimensional resonant tori; in this sense, 3DOF systems differ from 2DOF systems, in which periodic orbits and their associated families give phase space its structure. As the central concentration of the models is increased, boxlike phase space becomes more and more chaotic. A transition to global stochasticity occurs (§4) when the central mass contains between $\sim 2\%$ of the galaxy mass; for such large values of M_h , the boxlike phase space is almost completely stochastic, and diffusion takes place in a very short time. Interestingly, the critical black hole mass that we find for transition to global stochasticity is close to the maximum mass observed in real galaxies (Kormendy & Richstone 1995), and to the mass that induces a sudden evolution toward axisymmetry in N -body simulations (Merritt & Quinlan 1998). Central density cusps without black holes are less effective at generating chaos; even a modest black hole, with $M_h \approx 0.3\%M_g$, induces about as much stochastic diffusion as the steepest ($\rho \propto r^{-2}$) cusps.

Following Laskar (1993), we characterize the diffusion in phase space via the rate of change of the characteristic frequencies computed over a fixed interval of time. We find that the spectrum of diffusion rates at a given energy can be well approximated as a power law with slope close to -1 ; this spectrum extends over at least six decades (§5). Thus, every triaxial potential examined here has a significant population of slowly-evolving stochastic orbits. After a long enough time, even weakly stochastic orbits would be expected to contribute to chaotic mixing, an essentially irreversible process that leads to steady-state, invariant distributions in stochastic phase space. Once mixing sets in, triaxiality is likely to disappear, since regular box orbits are necessary for maintaining triaxial shapes. We estimate (§6) the timescale for this to take place as a function of galaxy luminosity; because typical orbital periods are shorter in faint ellipticals, they should be dynamically “more evolved” than bright ellipticals and hence less likely to maintain triaxial shapes. We predict evolution times that are roughly equal to galaxy lifetimes for elliptical galaxies with $M_B \approx -19$ to

–20, close to the absolute magnitude at which many elliptical galaxy properties – including the distribution of intrinsic shapes – are observed to change. We are therefore led to a picture (§7) in which many of the systematic differences between bright and faint ellipticals are a consequence of their different dynamical ages.

2 NUMERICAL TECHNIQUES

Laskar (1990) developed a new technique, the numerical analysis of fundamental frequencies (NAFF), for analyzing chaotic motion in the solar system. Laskar’s technique is based on the principle that an orbit in a system for which the motion is close to integrable is described by a well-defined set of frequencies ω_i , one per degree of freedom. For a regular orbit, the fundamental frequencies are invariant with respect to the coordinates in which the motion is represented. An analysis of the variation of the fundamental frequencies with respect to time enables one to detect the presence of chaos on shorter timescales than are usually possible with more classical techniques like Liapunov exponents. In addition, the NAFF algorithm allows one to quantify the degree to which a stochastic orbit has evolved over a given period of time; by contrast, Liapunov exponents reveal only the time-averaged rate of divergence in the vicinity of the orbit. A plot of the fundamental frequencies of a set of orbits drawn from a regular grid of initial conditions yields the “frequency map,” effectively a representation of the Arnold web of the system. The frequency map permits an identification of the resonant layers associated with stable and unstable motion as well as a determination of the size of the chaotic zones.

Laskar and collaborators have applied the NAFF algorithm to a wide variety of systems of astronomical and non-astronomical interest (Laskar 1990; Laskar, Froeschlé & Celletti 1992; Laskar 1993; Papaphilippou & Laskar 1996, 1998). These authors have shown that the frequency analysis technique is a remarkably powerful way to probe the structure of phase space in complex, non-integrable systems.

In the following subsections, we give a brief overview of Hamiltonian systems; summarize the basic principles of Laskar’s technique; and discuss several factors that affect the accuracy with which the fundamental frequencies can be recovered.

The models that we consider, both here and below, are “maximally triaxial” γ -models, i.e. they satisfy

$$\frac{a^2 - b^2}{a^2 - c^2} = \frac{1}{2}. \quad (4)$$

Henceforth we adopt units in which the total mass M , the x -axis scale length a , and the gravitational constant G are unity. The mass of the central black hole, when present, will be expressed as M_h ; since the total mass of the triaxial model is equal to one in our units, M_h may be interpreted as the mass of the black hole in units of the galaxy mass. Expressions for the gravitational potential and forces are given by Merritt & Fridman (1996). Following those authors, we assign orbits one of a set of 20 energies, defined as the values of the potential on the x -axis of a set of ellipsoidal shells -

with the same axis ratios as the density - that divide the model into 21 sections of equal mass. Thus shell 1 encloses 1/21 of the total mass, shell 2 encloses 2/21, etc.; shell 21 lies at infinity. The period of the x -axis orbit will often be used as a reference time; ω_0 is defined as $2\pi/T_x$, the frequency of the axial orbit.

2.1 Frequencies in Hamiltonian Systems

If a Hamiltonian system with N degrees of freedom (DOF) is integrable, the Hamiltonian $H(\mathbf{J}, \theta)$ can be written purely in terms of the N actions J_j , $H(\mathbf{J}, \theta) = H(J_j)$. The equations of motion of the system are then

$$\dot{J}_j = 0, \quad \dot{\theta}_j = \frac{\partial H}{\partial J_j} = \omega_j(\mathbf{J}), \quad (5)$$

for $j = 1, 2, \dots, N$. Orbits in the system can be written in terms of the complex variables

$$z_j(t) = J_j e^{i\theta_j} = z_j(0) e^{i\omega_j t}. \quad (6)$$

If $\partial\omega_j(\mathbf{J})/\partial J_j \neq 0$, the system is non-degenerate and in principle the actions can be written as

$$J_j = F_j(\omega_1, \omega_2, \dots, \omega_N). \quad (7)$$

When a system is integrable, the motion of a particle projected onto the (J_j, θ_j) plane describes pure circles. This is because the motion in phase space occurs on the surface of tori that are the products of true circles of radii $|J_j|$. The motion around a torus occurs at a rate determined by a frequency vector $(\omega_1, \omega_2, \dots, \omega_N)$ which is fixed for each torus. In general, we do not know the action-angle variables (J_j, θ_j) , but in restricted cases close approximations (J'_j, θ'_j) to these variables may be known. In these coordinates (J'_j, θ'_j) the motion is no longer pure circles but it is still determined by the same vector of frequencies $\theta'_j = \partial H/\partial J'_j = \omega_j(\mathbf{J})$ provided the new variables are canonically conjugate. The new coordinates may be written as a Laurent series expansion in terms of the action-angle variables $z_j(t)$:

$$\zeta(t) = z_j(t) + \sum_{\mathbf{m}} a_{\mathbf{m}} e^{i(\mathbf{m}\cdot\omega)t}. \quad (8)$$

In the limit that the coordinates (J'_j, θ'_j) are action-angle variables, the amplitudes $a_{\mathbf{m}}$ tend to zero.

Realistic systems with more than one DOF are rarely integrable, i.e. are rarely characterized by N global invariants. In some cases, the Hamiltonian can be written as a perturbation of an integrable Hamiltonian H_0 ,

$$H(\mathbf{J}, \theta) = H_0(\mathbf{J}) + \epsilon H_1(\mathbf{J}, \theta). \quad (9)$$

If the perturbation ϵ is small, the KAM theorem guarantees that a large fraction of the tori still persist and the motion of most of the orbits is still quasi-periodic. The motion on this discontinuous set of tori (defined by a Cantor set of frequency vectors $\Omega = (\omega_1, \omega_2, \dots, \omega_n)$ and therefore referred to as Cantori) is still describable in terms of action-angle variables. However it is no longer possible to define a single set of action variables that are valid over the entire phase space as in equation (7), since the frequencies change discontinuously

wherever the tori are destroyed. Nevertheless, fundamental frequencies continue to exist for all regular orbits.

A central role is played by the resonant tori, tori on which the fundamental frequencies satisfy a relation like $\mathbf{m} \cdot \boldsymbol{\omega} = 0$ where \mathbf{m} is a vector with integer components. The KAM theorem guarantees that “very nonresonant” tori – tori for which $\mathbf{m} \cdot \boldsymbol{\omega}$ is large – persist under small perturbation of any integrable Hamiltonian. Most of phase space is occupied by very nonresonant tori, but resonant tori are also dense in the phase space and do not survive small perturbations. Stable resonant tori (or “elliptic manifolds”) generate regions of regular motion while unstable resonant tori (“hyperbolic manifolds”) are often associated with stochastic layers. According to the Poincaré-Birkhoff theorem, elliptic and hyperbolic resonances come in pairs, leading to alternating regions of regular and stochastic motion. While resonant tori are dense in the phase space, only those of sufficiently low order – i.e., those with $|\mathbf{m}|$ sufficiently small – are likely to affect more than a very small phase space region. Resonances appear as lines in the frequency map, and the strength of a particular resonance is immediately apparent from the degree to which the otherwise-regular grid of points has been distorted (Laskar 1993).

In a 2 DOF system, motion on resonant tori is closed, since the resonance condition implies $\omega_1/\omega_2 = -m/l$ guaranteeing closure after m revolutions in θ_1 and l revolutions in θ_2 . It is therefore appropriate to state that the phase space of a 2 DOF system is structured by its periodic orbits. In a 3 DOF system, however, motion on resonant tori is not generally closed, since the single condition $\mathbf{m} \cdot \boldsymbol{\omega} = 0$ does not guarantee that any two of the three frequencies are commensurate. The resonance condition guarantees only that the trajectory inhabits a submanifold of dimensionality two on the 3-torus; closure requires the existence of an additional, independent resonance relation. While resonant tori continue to lend phase space its structure, one can not assign every regular orbit in a 3 DOF system to a family associated with a particular periodic orbit.

2.2 Numerical Recovery of the Fundamental Frequencies

Recovering the fundamental frequencies of a regular orbit is an aspect of “torus construction,” the derivation of the map that relates Cartesian and action-angle variables. Two general approaches to torus construction have been worked out in recent years. Iterative techniques (Chapman, Garrett & Miller 1976; Ratcliff, Chang & Schwarzschild 1984; McGill & Binney 1990; Warnock 1991; Binney & Kumar 1993; Kaasalainen & Binney 1994) begin by specifying the frequencies or actions of an orbit and then attempt to construct the relations $\mathbf{x}(\theta)$ that must be satisfied if the θ_i are to increase linearly with time. These methods are often elegant but suffer from a lack of robustness: the equations to be solved are nonlinear and convergence can depend sensitively on the accuracy of the initial guess. In a complex dynamical system containing many families of orbits, like the triaxial potentials considered here, it is generally necessary to “fine-

tune” the algorithms in order to achieve convergence in each distinct phase-space region (e.g. Kaasalainen 1995).

Trajectory-following algorithms (Boozer 1982; Kuo-Petravic et al. 1983) avoid these problems by making explicit use of the quasi-periodic nature of regular orbits. Quasi-periodicity guarantees that the motion in any canonical coordinate x can be expressed as

$$x(t) = \sum_{k=1}^{\infty} a_k e^{i\omega_k t} \quad (10)$$

where the ω_k are linear combinations of the fundamental frequencies, $\omega_k = l\omega_1 + m\omega_2 + n\omega_3$, and the a_k are complex amplitudes. By Fourier transforming the motion, the discrete peaks in the spectra can be identified as well as the corresponding amplitudes allowing a direct determination of $x(\theta)$. The actions then follow from Percival’s (1974) formula, completing the specification of the action-angle variables. Binney & Spergel (1982, 1984) pioneered this approach in the context of stellar dynamics, using a least squares technique to fit a model of the frequency spectra to $x(t)$.

Laskar’s (1990) trajectory-following approach, adopted here, achieves much greater accuracy. Laskar begins by replacing $x(t)$ in equation (10) by $f(t)$, some complex function of the orbit, e. g. $f(t) = x(t) + iv_x(t)$, which is similar to the function $\zeta(t)$ that appears in equation (8). A close approximation to $f(t)$,

$$f'(t) = \sum_{k=1}^N a'_k e^{i\omega'_k t}, \quad (11)$$

is then obtained in the following way. First, the time series $f(t)$ is translated to an interval $[-T/2, T/2]$ symmetric about the time origin. Next, a discrete Fourier transform is taken of f and the locations of the peaks ω'_k are identified. The position of any peak will be defined to an accuracy of $\sim 1/MT$ where M is the number of equally-spaced intervals at which f is recorded. The estimate of the location strongest peak is then refined by computing the maximum of the function

$$\phi(\omega) = \langle f(t), e^{i\omega t} \rangle = \frac{1}{T} \int_{-T/2}^{T/2} f(t) e^{-i\omega t} \chi(t) dt \quad (12)$$

where $\chi(t) = 1 + \cos(2\pi t/T)$ is the Hanning window function. The integral is approximated by interpolating the discretely-sampled f . The Hanning filter broadens the peak but greatly reduces the sidelobes, allowing a very precise determination of ω'_1 . Once the first frequency component has been found, its complex amplitude is obtained by projecting $e^{i\omega'_1 t}$ onto the original function $f(t)$, $a'_1 = \langle f(t), e^{i\omega'_1 t} \rangle$. The first term in the series is then subtracted, $f_1(t) = f(t) - a'_1 e^{i\omega'_1 t}$ and the process repeated on $f_1(t)$ to find the second frequency ω'_2 . In general, the functions $\mathbf{e}_1 = e^{i\omega'_1 t}$ and $e^{i\omega'_2 t}$ will not be orthonormal basis functions, but they can be made so by applying a Gram-Schmidt orthogonalization process to obtain \mathbf{e}_2 of the form $\mathbf{e}_2 = b_1 e^{i\omega'_2 t} - b_2 \mathbf{e}_1$, with b_1 and b_2 constants. \mathbf{e}_2 is then projected onto $f_1(t)$ to obtain the corresponding amplitude a'_2 . This process is repeated until the residual function does not significantly de-

crease following subtraction of another term. Typically, an accurate estimate of $f(t)$ is obtained with about 30 terms. We have found that extracting a larger number of terms from the function, while possible, does not always improve the accuracy with which the function $f(t)$ is estimated.

The frequency analysis of $f(t)$ yields a set of frequencies ω_k which are linear combinations of the fundamental frequencies $(\omega_1, \omega_2, \omega_3)$. Inferring the fundamental frequencies from the ω_k is an ill-defined problem, however, since any linearly-independent combination of the fundamental frequencies can equally well be interpreted as “fundamental.” Suppose that a particular spike in the frequency spectrum has $\omega_k = l\omega_1 + m\omega_2 + n\omega_3$. One can define new “fundamental frequencies” ω'_i as

$$\begin{aligned}\omega_1 &= n_{11}\omega'_1 + n_{12}\omega'_2 + n_{13}\omega'_3, \\ \omega_2 &= n_{21}\omega'_1 + n_{22}\omega'_2 + n_{23}\omega'_3, \\ \omega_3 &= n_{31}\omega'_1 + n_{32}\omega'_2 + n_{33}\omega'_3.\end{aligned}$$

In terms of these new frequencies, ω_k becomes

$$\begin{aligned}\omega_k &= (ln_{11} + mn_{21} + nn_{31})\omega'_1 + \\ &\quad (ln_{12} + mn_{22} + nn_{32})\omega'_2 + \\ &\quad (ln_{13} + mn_{23} + nn_{33})\omega'_3 \\ &= l'\omega'_1 + m'\omega'_2 + n'\omega'_3.\end{aligned}$$

In practice, one expects that the largest amplitude term in each frequency spectrum will correspond to a fundamental frequency. However, this is only guaranteed to be true if the coordinate in question is close to an angle variable.

This ambiguity turns out not to be serious in the case of boxlike orbits, which can be thought of as perturbed rectilinear orbits. The fundamental frequencies of a box orbit correspond approximately to motion in the x , y and z directions, and so a frequency analysis of the motion expressed in Cartesian variables yields highest-amplitude terms that can almost always be identified with fundamental frequencies. The same is not true for the tube orbits. For instance, the highest-amplitude term in both the x - and y -spectra of a short (z -) axis tube orbit is typically associated with the frequency of rotation around the z axis, ω_ϕ . The term of next highest amplitude typically has a frequency of $\omega_R - \omega_\phi$, with ω_R the fundamental frequency associated with motion in the radial direction.

Despite these complications, we have successfully used an automated, integer-programming “branch and bound” algorithm from the NAG library (H02BBF) to extract the fundamental frequencies from the frequency spectra. The entire set of frequencies ω_k is first sorted in descending order of their real amplitudes. The frequency component of highest amplitude is defined to be the first fundamental frequency ω_1 . The entire series is then searched in descending order of amplitude to find the second fundamental frequency ω_2 , defined as the first term in the series which is not a simple integer multiple of ω_1 . The integer programming routine then defines as ω_3 the next frequency component that is not a linear combination of ω_1 and ω_2 . In the case of box orbits and most tube orbits, the error in identifying the fundamental frequencies, $\text{err}(\omega_k) = |\omega_k - (l_k\omega_1 + n_k\omega_2 + m_k\omega_3)|$, is less than about 10^{-5} . Papaphilippou & Laskar (1996) showed

that polar coordinates were better suited than Cartesian coordinates to obtaining the fundamental frequencies of tube orbits in an unambiguous way. However, we found that an analysis of the tube orbits in terms of Cartesian coordinates was satisfactory. Two of the “fundamental frequencies” of a tube orbit returned by the integer programming routine could almost always be interpreted as ω_ϕ and $\omega_R - \omega_\phi$, as discussed above; the third frequency corresponded to motion in a direction parallel to the symmetry axis of the tube.

Once the fundamental frequencies are obtained, one can define the frequency map, a map from initial condition space to the space of fundamental frequencies. Since all orbits from a given ensemble were selected to have the same energy, the distribution of points in frequency space defines a two-dimensional surface; we follow the practice of Laskar and co-authors of plotting ω_1/ω_3 vs. ω_2/ω_3 . As discussed above, regular regions in the frequency map are often associated with resonances between the fundamental frequencies, $\mathbf{m} \cdot \boldsymbol{\omega} = 0$. The highest-amplitude terms in the frequency spectrum of an orbit near a stable resonance typically reflect the resonance condition. For instance, near the $x - z$ “banana” orbit, which has $\omega_x/\omega_z = 1/2$, one typically finds $\omega_1/\omega_3 = 0.5$ with very high accuracy. An additional frequency, associated with the slow libration around the resonance, is also present in the spectrum but is generally small ($< 10^{-6} \times \omega_1$) and of such low amplitude that it is not selected by the integer-programming routine. We again follow the practice of Papaphilippou & Laskar (1996, 1998) of defining the fundamental frequencies in the vicinity of a resonance as the frequencies corresponding to the highest-amplitude terms. Thus, at least two of the fundamental frequencies of orbits in an island around a boxlet will remain in exact proportion as one moves across the island; the frequency corresponding to slow libration is ignored. This practice results in the set of orbits around a stable resonance mapping into a line in the frequency map, a very convenient representation.

Stochastic orbits are not quasi-periodic and hence their frequency spectra can not be interpreted in terms of just three fundamental frequencies. However, if an orbit is only weakly stochastic, the integer programming routine will still yield a set of “fundamental frequencies” in terms of which the various peaks in the frequency spectrum can be expressed with more or less accuracy. As the degree of stochasticity increases, these “fundamental frequencies” become simply the three ω_k corresponding to the three strongest peaks in the frequency spectrum. So defined, the “fundamental frequencies” of a stochastic orbit will depend on the time interval over which the orbit was integrated. By integrating a stochastic orbit over two successive time intervals $[0, T]$, $[T, 2T]$, one can compute the change in these frequencies, which is a measure of the rate of diffusion in frequency space (Laskar 1993).

In the remainder of the paper we will refer to our algorithm for carrying out the frequency analysis and integer programming as “NAFF,” even though it differs slightly from Laskar’s algorithm.

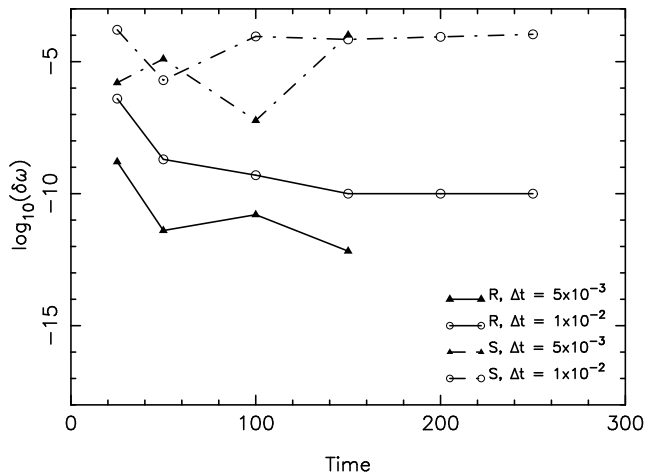


Figure 1. Dependence of Laskar’s bootstrap accuracy estimate $\delta\omega = |\omega'' - \omega'|$ on the orbital integration time. The solid lines are for a regular orbit, with the time series sampled at two different intervals Δt as indicated. The broken lines are for a stochastic orbit.

2.3 Accuracy of the NAFF Algorithm

In this section, we discuss some of the factors that affect the accuracy with which the fundamental frequencies of an orbit can be recovered.

Orbits were integrated using an explicit Runge-Kutta scheme of order 8 based on the method of Prince & Dormand (1981). The program DOP853 from Hairer, Norsett & Wanner (1993) uses local error estimation and adaptive step size control based on embedded formulas of orders 5 and 3 respectively. An important feature of the code is its ability to produce “dense output,” accurate estimates of the dependent variables at time intervals much shorter than the integration time step. The program DOP853 produces dense output via 7th-order interpolation between the output points. The dense output option greatly speeded up the construction of the time series needed for the frequency analysis routine.

In order to estimate the accuracy of the numerically-computed ω_i , Laskar (1993) suggested the following bootstrap scheme. Call $f'(t)$ the numerical approximation of the original time series $f(t)$, as in equation (11). Carry out a second frequency analysis of $f'(t)$. The result is

$$f''(t) = \sum_{k=1}^N a_k'' e^{i\omega_k'' t}. \quad (13)$$

Then $\delta a_k = |a_k'' - a_k'|$ and $\delta\omega_k = |\omega_k'' - \omega_k'|$ are estimates of the precision with which a_k' and ω_k' have been determined.

Laskar (1996) has shown that frequency analysis with a Hanning filter yields estimates of the fundamental frequencies whose accuracies scale asymptotically as $1/T^4$, with T the integration interval. For an ordinary FFT the dependence is only $1/T$. Two additional factors affecting the accuracy of the recovered frequencies are the sampling interval

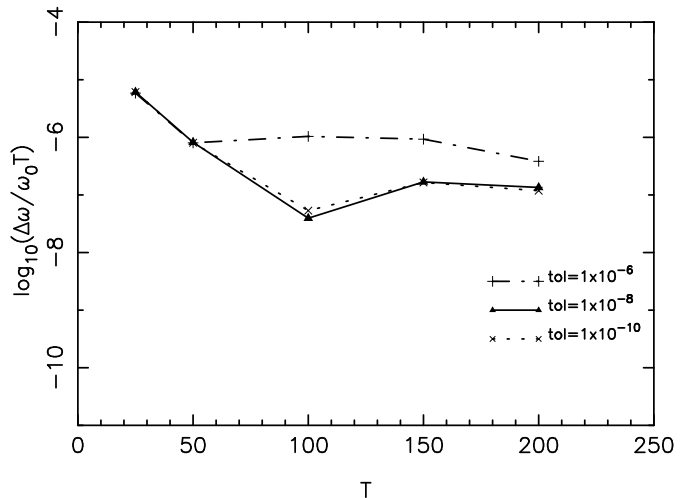


Figure 2. Diffusion rate $\Delta\omega$ obtained by measuring the frequencies of a regular orbit over two successive time intervals of length T , plotted as a function of T , for three different values of the tolerance parameter of the orbit integrator.

Δt and the accuracy of the numerical integrator. We estimated the accuracy of the NAFF routine by applying it to two orbits in a γ -model with $c/a = 0.5$ and $\gamma = 0.5$. Figure 1 shows how the error in the fundamental frequencies of two different orbits varies with T and Δt ; the time unit is the period of the long-axis orbit of the same energy. $\delta\omega$ was defined as $|\omega'' - \omega'|$ for the frequency component of the largest amplitude. The solid lines were obtained for a regular orbit, and the broken lines were obtained for a stochastic orbit. The open circles correspond to a larger sampling interval of $\Delta t \sim 10^{-2}$ (~ 100 steps per orbital period) and the filled circles correspond to a smaller sampling interval of $\Delta t \sim 5 \times 10^{-3}$ (~ 200 steps per orbital period). This figure illustrates the reduction in $\delta\omega$ for a regular orbit as the integration interval is increased. The smaller sampling interval also improves the bootstrap estimate of the accuracy $\delta\omega$ by nearly two orders of magnitude. In the rest of the paper we adopt an integration interval of 50 orbital periods (defined as the period of the long-axis orbit of the same energy) and a sampling interval $\Delta t = 5 \times 10^{-3}$. Figure 1 also shows that the “frequencies” of a stochastic orbit are obtained with a much lower accuracy ($10^{-4} - 10^{-6}$) than for a regular orbit. Clearly, the function $f'(t)$ obtained for a stochastic orbit is not a good approximation to the original $f(t)$.

Another way to estimate the accuracy of the NAFF routine is to integrate a single, regular orbit over two successive time intervals and compare the estimates of the fundamental frequencies. We define $\Delta\omega = |\omega(T_1) - \omega(T_2)|/\omega_0 T$, where T_1 and T_2 are the midpoints of the two intervals, $T = T_2 - T_1$, and $\omega_0 = 2\pi/T_X$, the frequency of the long-axis orbit of the same energy. Figure 2 shows $\Delta\omega$ as a function of T and of the tolerance parameter of the numerical integrator for the regular orbit of Figure 1. Figure 2 indicates that decreasing the tolerance parameter below 1×10^{-8} does not significantly affect the value of $\Delta\omega$ when the sampling interval is fixed to

this value. Unless otherwise indicated, results in this paper were obtained with a tolerance parameter of 10^{-8} .

3 THE STRUCTURE OF PHASE SPACE

We begin by looking in detail at a triaxial γ -model with $c/a = 0.5$ and $\gamma = 0.5$, a “weak cusp.” Two ensembles of $\sim 10^4$ orbits were integrated in this model at the fixed energy corresponding to shell 8, which lies just inside the half-mass radius. Initial conditions for the two ensembles were chosen so as to generate either boxlike orbits or tube orbits; i.e. orbits with stationary points, or orbits that circulate about one of the principal axes of the model. (A more complete discussion of the two initial-condition spaces may be found in Merritt & Fridman 1996). Orbits were integrated for a total of 100 periods of the x -axis orbit. Fundamental frequencies were computed independently for the first and second halves of this interval so that diffusion rates could be calculated, as described above.

3.1 Box-Orbit Initial Conditions

A large part of the phase space of a triaxial system is associated with orbits that have a stationary point, i.e. that touch the equipotential surface with zero velocity. All of the box orbits in an integrable (Stäckel) potential fall into this category, as do the “centrophobic” boxlets, like the $x-z$ banana, in non-integrable potentials. (“Centrophilic” boxlets, like the anti-banana, typically do not have a stationary point. Such orbits are generally unstable (Miralda-Escudé & Schwarzschild 1989)). In Figure 3, the NAFF algorithm has been applied to a set of 9408 orbits whose initial conditions lay in a regular grid on one octant of the equipotential surface corresponding to shell 8. Figure 3a presents a planar projection of the initial condition space; the gray scale has been adjusted in proportion to the logarithm of the diffusion rate, defined as the change in the largest-amplitude fundamental frequency as evaluated over the initial and final intervals of 50 periods each. Figure 3b is the frequency map corresponding to the first integration interval. In both figures, resonances defined by $l\omega_x + m\omega_y + n\omega_z = 0$ have been identified for certain integer values of (l, m, n) .

The frequency map exhibits some regions in which the points are arranged in a more-or-less orderly fashion. These regions may be identified with parts of phase space that have retained their regular character in spite of the perturbation of the potential away from integrable, or Stäckel, form. Separating these regular regions are the resonance lines: either solid lines, corresponding to stable resonant tori; or empty gaps, corresponding to stochastic layers. In addition, a number of points are scattered in a more irregular manner around the figure. These are the stochastic orbits. However, even the stochastic orbits are mostly clustered around resonance lines, indicating that the stochastic motion is often strongly influenced by structures in phase space that are similar to invariant tori.

The short ($z-$), intermediate ($y-$) and long ($x-$) axis orbits are all unstable to lateral perturbations at this energy

in this potential (Fridman & Merritt 1997). Instability of the $z-$ axis orbit first occurs at low energy through bifurcation of the $1 : 1$ $y-z$ loop orbit (Goodman & Schwarzschild 1981). The influence of this resonance is visible at the top of Figure 3b, where many of the stochastic orbits started near the z axis are clustered around the $(0, 1, -1)$ resonance line. (The stable branch of the bifurcation, the $y-z$ loop orbits, do not appear in this plot since they have no stationary points.) Instability of the $y-$ axis orbit first occurs through the $1 : 1$ $x-y$ loop bifurcation; the region around the $(1, -1, 0)$ resonance is also well populated in the frequency map, by stochastic orbits that start near the $y-$ axis. Finally, the $x-$ axis orbit becomes unstable at the bifurcation of the $1 : 2$ $x-z$ banana orbit, which occurs at about shell 2 in this model (Fridman & Merritt 1997). Unlike the $1 : 1$ loop orbits, however, the stable banana orbit does lie in stationary initial condition space, and hence the family of stable orbits generated by the bifurcation appear in the frequency map along the $(2, 0, -1)$ resonance line. A smaller number of stochastic orbits lie near to, but offset from, the $(2, 0, -1)$ line.

As emphasized by Papaphilippou & Laskar (1998), the motion in boxlike phase space is strongly influenced by resonances between the three degrees of freedom. Such resonances are dense in the phase space of an unperturbed, i.e. integrable, Hamiltonian, in the sense that every torus lies near to a torus satisfying $\mathbf{m} \cdot \boldsymbol{\omega} = 0$ for some (perhaps very large) integer vector \mathbf{m} . However, most tori are very non-resonant in the sense that $\mathbf{m} \cdot \boldsymbol{\omega}$ is large compared with $|\mathbf{m}|^{-(N+1)}$, with N the number of degrees of freedom. These very non-resonant tori persist under finite perturbations of the Hamiltonian and may be identified with the orderly regions between the resonance lines in the frequency map of Figure 3b. Resonant tori, particularly those with small \mathbf{m} , are either destroyed by a finite perturbation, generating stochastic motion, or become associated with a regular region surrounding the resonance, or (typically) both. Many – perhaps most – of the regular orbits in Figure 3a can be identified with a stable resonance; among the most important are the $(2, 1, -2)$, $(3, -1, -1)$, and $(4, -2, -1)$ resonances. The intersection of any two resonance lines defines a periodic orbit, i.e. an orbit for which $\omega_x/\omega_z = l/n$ and $\omega_y/\omega_z = m/n$. When stable, a periodic orbit can have its own associated regular region, distinct from the regular regions associated with the 3D resonances. At least two such regions are apparent in Figure 3a, associated with the $5 : 6 : 8$ and $7 : 9 : 10$ periodic orbits (marked 1 and 2). In addition, the $x-z$ fish ($2 : 3$) and $x-y$ pretzels ($3 : 4$) planar boxlets have associated regular regions.

It is sometimes stated that all of the regular orbits in a galactic potential belong to families that can be associated with stable periodic orbits. For instance, the box orbits in a Stäckel potential are commonly associated with the long-axis orbit, while the tube orbits are said to belong to families generated by the $x-y$ or $y-z$ $1 : 1$ planar loops. While the identification of regular orbits with stable periodic orbits is sometimes justified, only a small fraction of the regular orbits in Figure 3a can be usefully assigned to families associated with periodic orbits. A larger fraction of

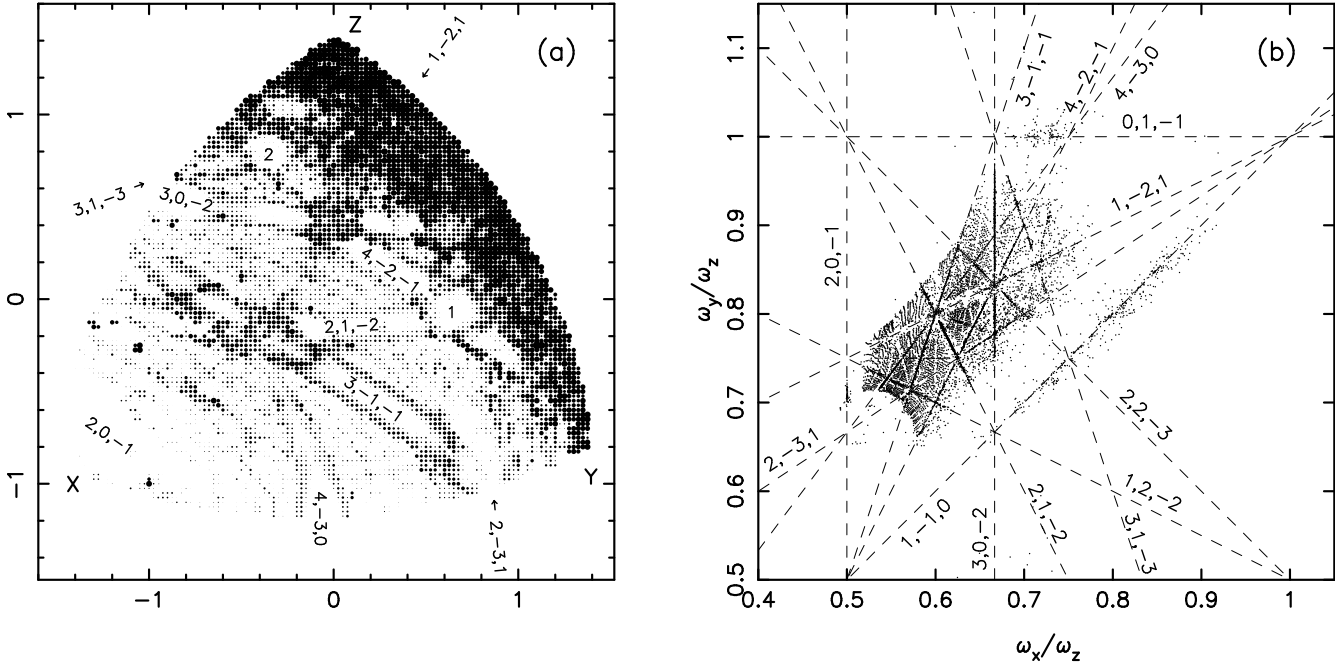


Figure 3. Box-orbit phase space at shell 8 in the model with $\gamma = 0.5$. (a) Initial condition space: one octant of the equipotential surface has been projected onto a plane. Each orbit begins on this surface with zero velocity. The top, left and right corners correspond to the z (short), x (long) and y (intermediate) axes. The grey scale is proportional to the logarithm of the diffusion rate of orbits in frequency space; initial conditions corresponding to regular orbits are white. The regions labelled “1” and “2” contain orbits associated with the $5 : 6 : 8$ and $7 : 9 : 10$ periodic orbits, respectively. Other regions are labelled with the integers (l, m, n) that define resonance zones. (b) Frequency map: the fundamental frequencies returned by the NAFF algorithm are plotted as rotation numbers ω_x/ω_z and ω_y/ω_z for each of the orbits in (a). The most important resonances are labelled. Stable resonances produce solid lines; gaps correspond to unstable resonances.

the regular orbits are located in resonance *zones*, regions associated with tori that satisfy a single resonance condition $l\omega_x + m\omega_y + n\omega_z = 0$. We expect orbits in such regions to be approximately confined to two-dimensional sub-manifolds; in configuration space, they should take the form of thin, curved sheets. An example of such an orbit, which we call a “thin box,” is shown in Figure 4. Closure requires an additional resonance condition $\mathbf{m} \cdot \boldsymbol{\omega} = 0$ to be satisfied so that the frequency vector can be written as $\boldsymbol{\omega} = \mathbf{n}\omega_0$ with \mathbf{n} an integer vector.

In initial condition space (Figure 3a), the regions associated with stable resonance zones appear as bands of white, flanked on both sides by narrower stochastic strips. Periodic orbits lie at the intersection of two or more of these bands, and some of these periodic orbits – e.g. the $5 : 6 : 8$ and $7 : 9 : 10$ orbits in Figure 3a – are surrounded by regions in which the motion is regular. Orbits in these restricted regions may be usefully associated with the periodic orbit at their center. But Figure 3a suggests that the regular regions associated with stable periodic orbits are relatively small, and they are often separated from the larger regular regions by strips where the motion is stochastic. There would seem to be no reason to associate the regular motion in the largest part of any resonance zone with any particular periodic orbit.

In a 2 DOF system, the condition $l\omega_1 + m\omega_2 = 0$ that defines a resonant torus also defines a periodic orbit, since $\omega_1/\omega_2 = -m/l$ implies commensurability of the motion in the two directions around the torus. The distinction between periodic orbits and resonant tori therefore does not appear in systems with fewer than three degrees of freedom. In the same way, it is clear from Figure 3a that orbits restricted to, say, the $x - y$ plane are affected by the $(4, -3, 0)$ resonance zone only where that zone intersects the $x - y$ plane, at the $x - y$ pretzel orbit. In the case of the majority of non-planar regular orbits, however, no unique identification with a periodic orbit is possible.

In addition to the regular orbits associated with resonance zones and with periodic orbits, a third class of regular orbit is apparent in Figure 3. These are orbits that lie in the (essentially) completely regular regions that lie between the resonance zones. Orbits in these regions may be identified with very non-resonant tori, i.e. tori that have maintained their integrity in spite the perturbation of the Hamiltonian away from integrable form. In an integrable potential, all of the regular orbits would belong to such regions; in a non-integrable potential, only tori that are sufficiently non-resonant are expected to avoid being strongly deformed by the perturbation. Strictly speaking, we expect to find some high-order resonance zones and associated stochastic

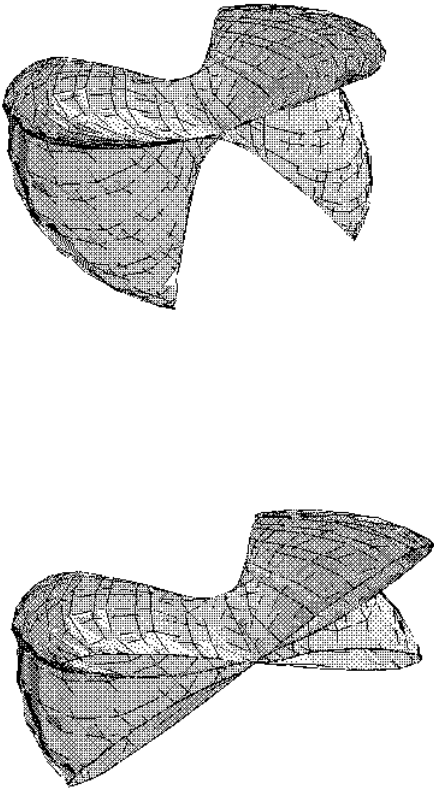


Figure 4. A thin box orbit associated with the $(2, 1, -2)$ resonance. The lower view is a cutaway showing that the orbit is confined to a membrane.

regions imbedded within even these “regular” regions, and in fact a close inspection of Figure 3a reveals just such structure. However, the chaotic diffusion rates in these regions are generally small and for practical purposes the motion in them is effectively regular throughout. Again, we note that the motion in one of these regular regions can not be properly identified with any single periodic orbit; instead, the regularity of the motion would seem to be properly identified with the persistence of integrability in extended, non-resonant parts of phase space in spite of the perturbation of the Hamiltonian away from fully integrable form.

An equivalent way to define the three “types” of regular orbit described above is in terms of the number of independent relations $\mathbf{m} \cdot \boldsymbol{\omega} = 0$ that characterize their associated phase space regions, i.e. in terms of the degeneracy of the resonance. A periodic orbit is defined by two such relations; a resonance zone by one; and the regular regions that persist in spite of the perturbation of the potential away from integrability are defined by none. It is clear from this definition that the number of distinct “types” of regular orbit is equal to the number of degrees of freedom. While regular orbits of all three types occupy three-dimensional regions in configuration space, orbits associated with a single resonance condition are approximately confined to sheets, while orbits associated with two resonance conditions are approximately confined to closed curves.

Given that essentially none of the boxlike orbits in Fig-

ure 3a can be properly identified with the long-axis orbit, it is reasonable to ask in what sense the box orbits in *any* triaxial potential – even that of the Perfect Ellipsoid – are correctly said to belong to the “family of orbits” associated with the long-axis orbit. We would argue instead that the regularity of the box orbits in a Stäckel potential is properly ascribed to the global integrability of the potential, and not to the local stability of any single periodic orbit like the long-axis orbit.

The regions corresponding to stochastic motion in Figure 3a can likewise be separated into three fairly distinct types, with one important qualification. Stochastic orbits live in a phase space of higher dimensionality than regular orbits, and in fact we expect every stochastic orbit to eventually visit (via Arnold diffusion) every point of phase space, even points that are arbitrarily close to regular orbits. However the timescale for Arnold diffusion is extremely long, and for practical purposes, stochastic orbits – like regular orbits – can often be associated with restricted parts of phase space. Accordingly, in Figure 3a, we identify three “types” of stochastic orbit. First are the stochastic orbits closely associated with an unstable periodic orbit. An example is the region around the $4 : 5 : 6$ periodic orbit that lies at the intersection of the $(3, 0, -2)$ and $(4, -2, -1)$ resonance zones. Second, some stochastic orbits lie along the edges of the stable resonance zones, as mentioned above. Third, there is a large stochastic strip connecting the y - and z -axis orbits. Goodman & Schwarzschild (1981) first described this stochastic strip in their study of stochastic motion in a triaxial model with a core. The overlap of the chaotic zones associated with the y and z -axis orbits appears to be responsible for most of this strip, although a number of other resonances are also important, including especially the $(1, -2, 1)$ resonance. Although the diffusion rate of orbits in the stochastic strip is high, we would not expect these orbits to wander ergodically over the entire energy surface due to the existence of substantial regular regions which would inhibit the diffusion. However, the near constancy of the diffusion rate throughout the $y - z$ strip suggests that the motion is nearly ergodic over this restricted region, at least for elapsed times of $\sim 10^2$ oscillations or more.

3.2 Tube-Orbit Initial Conditions

The other major category of orbits in a triaxial potential, the tube orbits, are characterized by a finite, time-averaged angular momentum about the long or short axis. In an integrable triaxial potential, the three families of tube orbits – the short-axis tubes, the inner long-axis tubes, and the outer, long-axis tubes – can all be recovered by taking initial conditions in the $x - z$ plane, with $v_y = 0$ (Schwarzschild 1993). This initial condition space will also include some box orbits. Figure 5a presents the $x - z$ initial condition space for the same model of Figure 3; again, the grey scale is adjusted in proportion to the logarithm of the diffusion rate. The corresponding frequency map is shown in Figure 5b. Any non-periodic orbit intersects the $x - z$ plane in at least two points; in the case of tube orbits, the two points lie in-

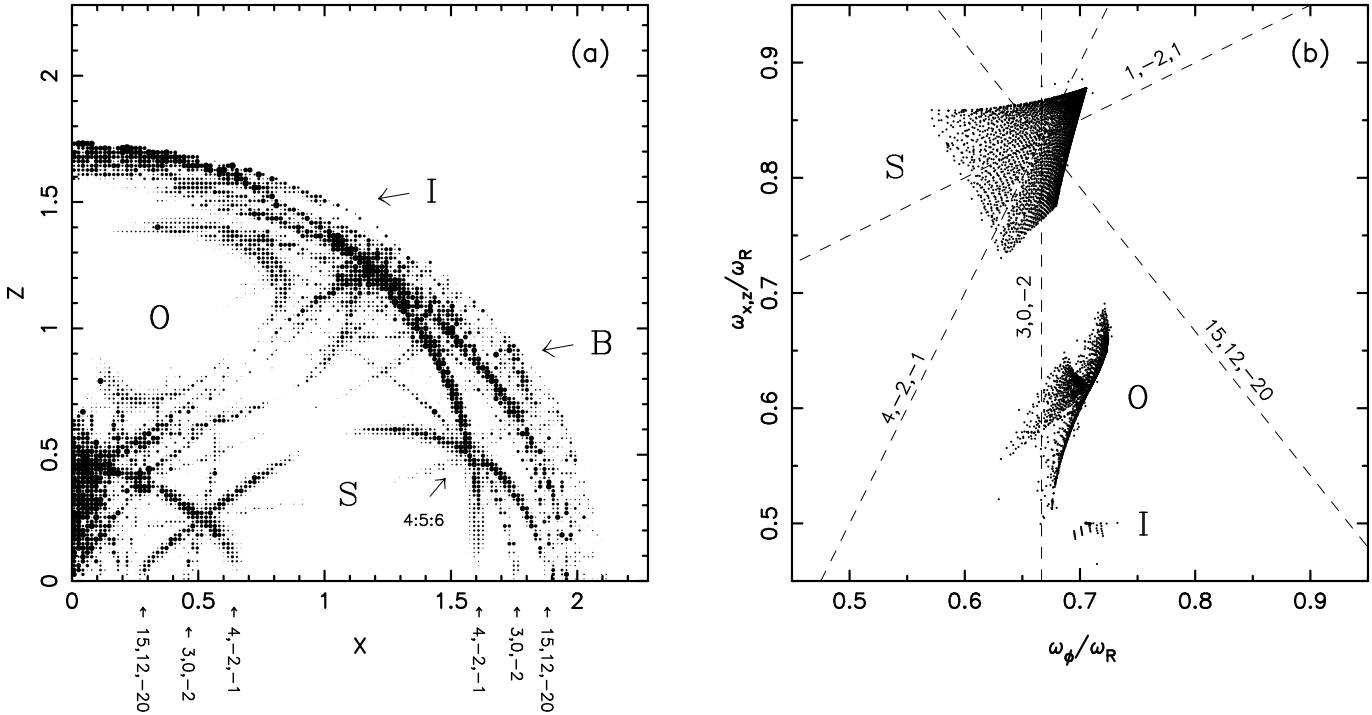


Figure 5. Tube-orbit phase space at shell 8 in the model with $\gamma = 0.5$. (a) Initial condition space: orbits begin on the $x - z$ plane with $v_x = v_z = 0$. The grey scale is proportional to the logarithm of the diffusion rate of orbits in frequency space; initial conditions corresponding to regular orbits are white. The regions labelled “S,” “O,” “I” and “B” contain short-axis tubes, outer long-axis tubes, inner long-axis tubes and boxes, respectively. The three most important resonance zones are labelled; they intersect at the (unstable) 4 : 5 : 6 orbit (Figure 6). (b) Frequency map, with the important resonances labelled. Only the tube orbits are included. ω_ϕ is the fundamental frequency associated with motion about the short axis (short-axis tubes), or long axis (long-axis tubes).

side and outside the curve that defines the corresponding “thin” orbit family.

As discussed above, the highest-amplitude components in the x - and y - spectra of a short (z -) axis tube are typically both associated with the frequency of rotation about the z axis, ω_ϕ ; the frequency corresponding to radial oscillations, ω_R , appears typically in terms of much lower amplitude. For a few of the $\sim 10^4$ tube orbits integrated here, the automated routine for extracting fundamental frequencies appeared to fail, leaving some random gaps in the frequency map of Figure 5b. (Papaphilippou & Laskar (1996) reported similar difficulties in their analysis of tube orbits.) However, the fundamental frequencies of the great majority of regular tube orbits were successfully recovered. In Figure 5b, only orbits that clearly belonged to one of the three tube families are plotted in the frequency map; the boxlike orbits are omitted for clarity. The fundamental frequency labeled ω_ϕ is defined as the frequency associated with motion around the z axis in the case of the short-axis tubes (labeled “S” in the figure), and as the frequency associated with motion around the x axis in the case of the inner (I) and outer (O), long-axis tubes.

This part of phase space is largely regular. Aside from the box orbits, which are confined to regions near the zero-velocity curve, all stochastic tube orbits are associated with a handful of narrow resonance zones. These zones exist at

the transition points between the various families, as noted by Merritt & Fridman (1996) and Papaphilippou & Laskar (1998). A few additional resonances are important, including the (4, -2, -1), (3, 0, -2) and the surprisingly high-order (15, 12, -20) resonance. These three resonances intersect at the 4 : 5 : 6 periodic orbit, an unstable tubelet (Figure 6). The diffusion rates appear to drop to zero along the curve defining the thin tube orbits belonging to the *S* and *O* families, a reasonable result.

We have encountered little discussion in the literature of stochastic tube orbits; the nearest examples that we know of are orbits that Kandrup, Eckstein & Bradley (1997) describe as appearing “alternately boxy and loopy.” Accordingly, we illustrate in Figure 7 the evolution of a tube orbit associated with the unstable (4, -2, -1) resonance zone in Figure 5a. The orbit was integrated for three successive intervals equal to 50 periods of the long-axis orbit. The stochasticity is evident in the gradual change of the orbit’s shape. Assuming that the entire stochastic phase space at this energy is interconnected, we would expect this tube orbit to eventually find its way into boxlike phase space. However the time required is likely to be extremely long, since the diffusion would have to occur along the (4, -2, -1) resonance line, and diffusion along resonance layers – i.e. Arnold diffusion – is known to be extremely slow.

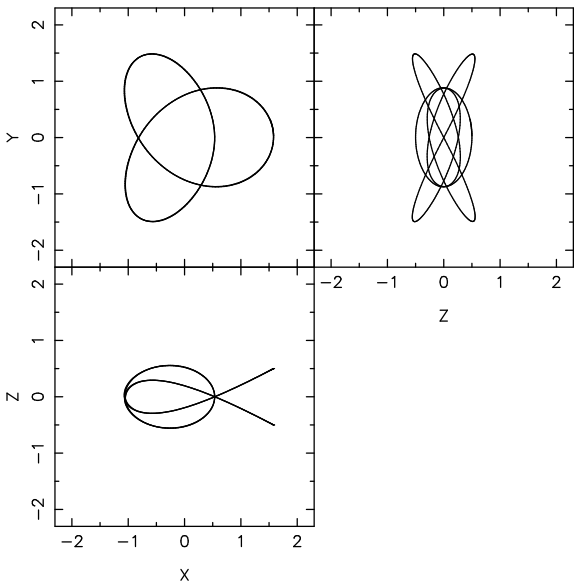


Figure 6. The unstable, 4 : 5 : 6 resonant tube orbit that appears in Figure 5

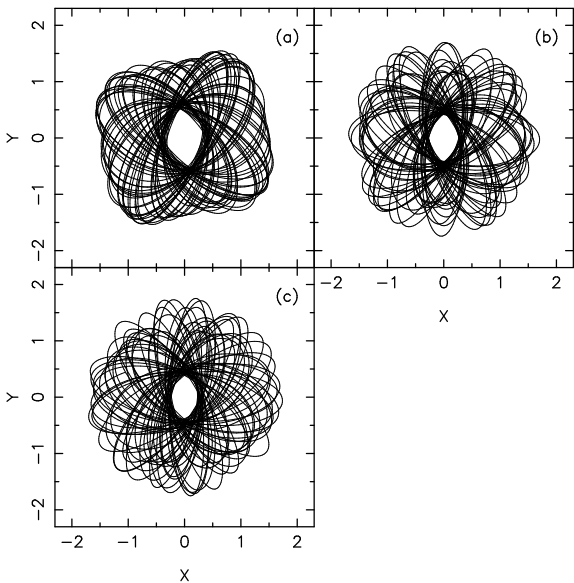


Figure 7. A stochastic, short-axis tube orbit. The initial conditions lie in Figure 5a on the resonance zone labelled (4, -2, 1), slightly above the 4 : 5 : 6 periodic orbit. (a), (b) and (c) show three successive integrations of the orbit, each over a time span of 50 periods of the long-axis orbit.

4 THE TRANSITION TO GLOBAL STOCHASTICITY

When an integrable potential is perturbed by increasingly large amounts, the fraction of phase space associated with stochastic motion and the rate of stochastic diffusion typically increase. In triaxial γ -models, the parameter γ that defines the steepness of the central density cusp is expected to play the role of a perturbation parameter: models with

γ close to zero should be close to integrable (though never exactly so, since the γ -models do not reduce to integrable form even for $\gamma = 0$), while values of γ greater than about one are known to generate strongly stochastic motion (Merritt & Fridman 1996). The mass of a central singularity, and the energy, should also act as perturbation parameters; for instance, the long-axis orbit generally becomes unstable at sufficiently high energies even in triaxial potentials with cores. In terms of any of these perturbation parameters, box-like phase space should be most strongly affected since tube orbits avoid the destabilizing center.

In the case of extreme perturbations, dynamical systems sometimes exhibit a transition to global stochasticity, a regime in which the stochastic motion is interconnected over large portions of the phase space. (Strictly speaking, stochastic phase space in a 3 DOF system is always interconnected through the Arnold web, but Arnold diffusion is extremely slow unless the stochastic regions overlap.) In the globally stochastic regime, there are few barriers to the motion and orbits can wander over the energy hypersurface in little more than an orbital period. One standard definition of the transition to global stochasticity is based on the overlap of the stochastic layers associated with the primary resonances (Chirikov 1960). Other definitions (Lichtenberg & Lieberman 1992) are based on the fraction of phase space that is stochastic, the degree to which the stochastic regions are interconnected, etc.

In triaxial stellar systems, a transition to global stochasticity implies the replacement of distinguishable box orbits by orbits that move nearly ergodically over the energy surface and that densely fill the configuration space volume defined by an equipotential surface. Since box orbits with various shapes are always found to be strongly populated in self-consistent triaxial models (Schwarzschild 1979; Statler 1987), significant triaxiality should be difficult or impossible to maintain in a system where the motion is globally stochastic. This hypothesis has received some support from self-consistent equilibrium studies (Schwarzschild 1993; Merritt 1997) and from N -body integrations (Merritt & Quinlan 1998).

We investigated the approach to global stochasticity in the triaxial γ -models by applying the NAFF algorithm to a set of models with different values of the central density slope γ and with central point masses M_h of various sizes. (Dependence of the degree of stochasticity on the energy is discussed in the following section.) In each model, we integrated ensembles of $\sim 10^4$ orbits at shell 8 in boxlike initial condition space and computed their fundamental frequencies over two adjacent time intervals with the NAFF algorithm. We carried out similar experiments in the initial condition space of tube orbits; however, as expected, the degree of stochasticity was not found to depend strongly on the central density structure and so those results will not be presented here.

Figures 8 and 9 show the diffusion rates and frequency maps for ensembles of orbits with boxlike initial conditions in a set of γ -models with five different values of γ between 0 and 2 and $c/a = 0.5$. The density cusps in real elliptical galaxies are almost always found to have slopes that lie in

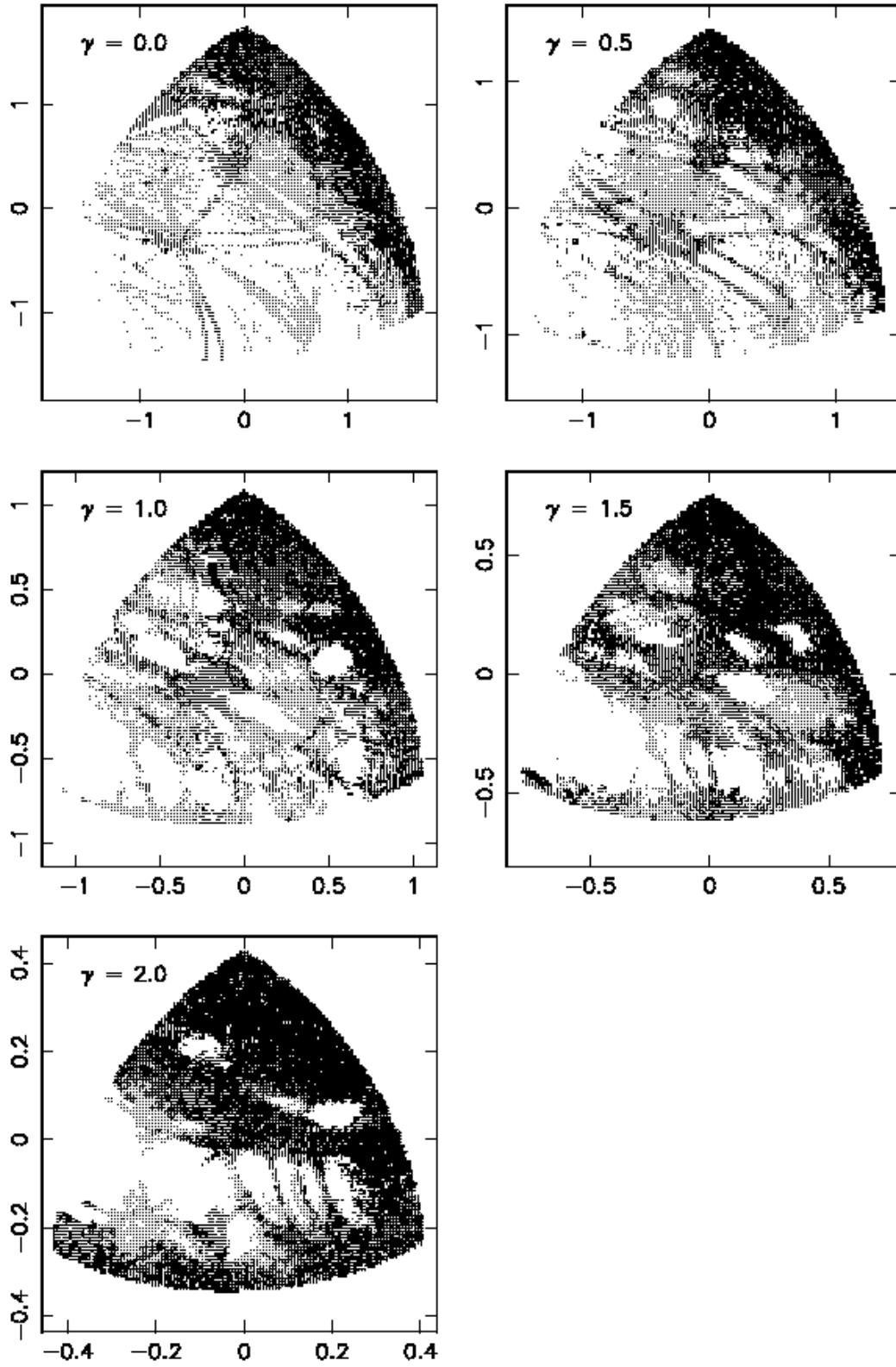


Figure 8. Initial condition space at shell 8 in a set of models with various values of the cusp slope γ . The grey scale is proportional to the logarithm of the diffusion rate in frequency space, defined as the fractional change in the largest-amplitude fundamental frequency over 50 periods of the long-axis orbit. White regions correspond to regular orbits.

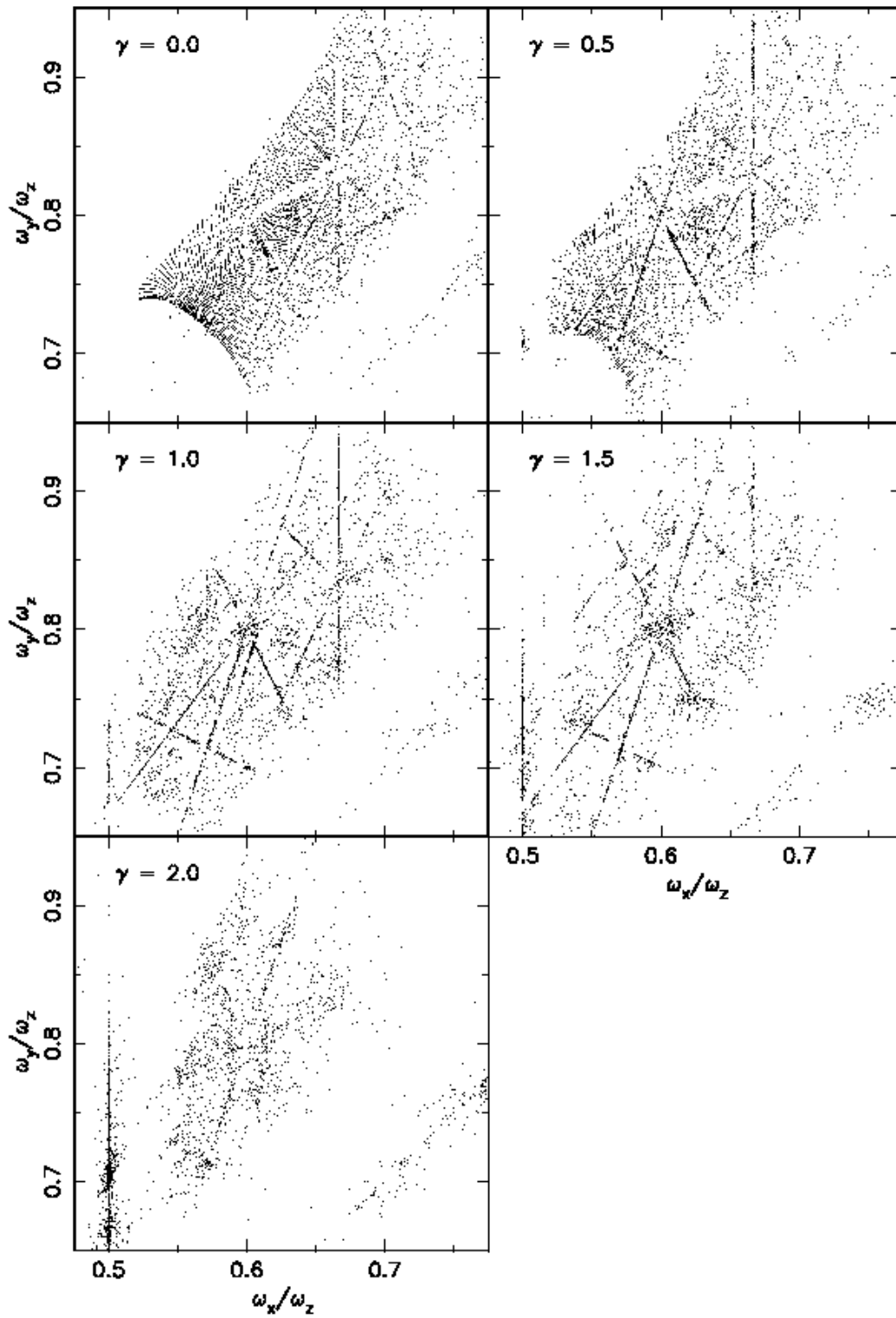


Figure 9. Frequency maps for the orbits of Figure 8.

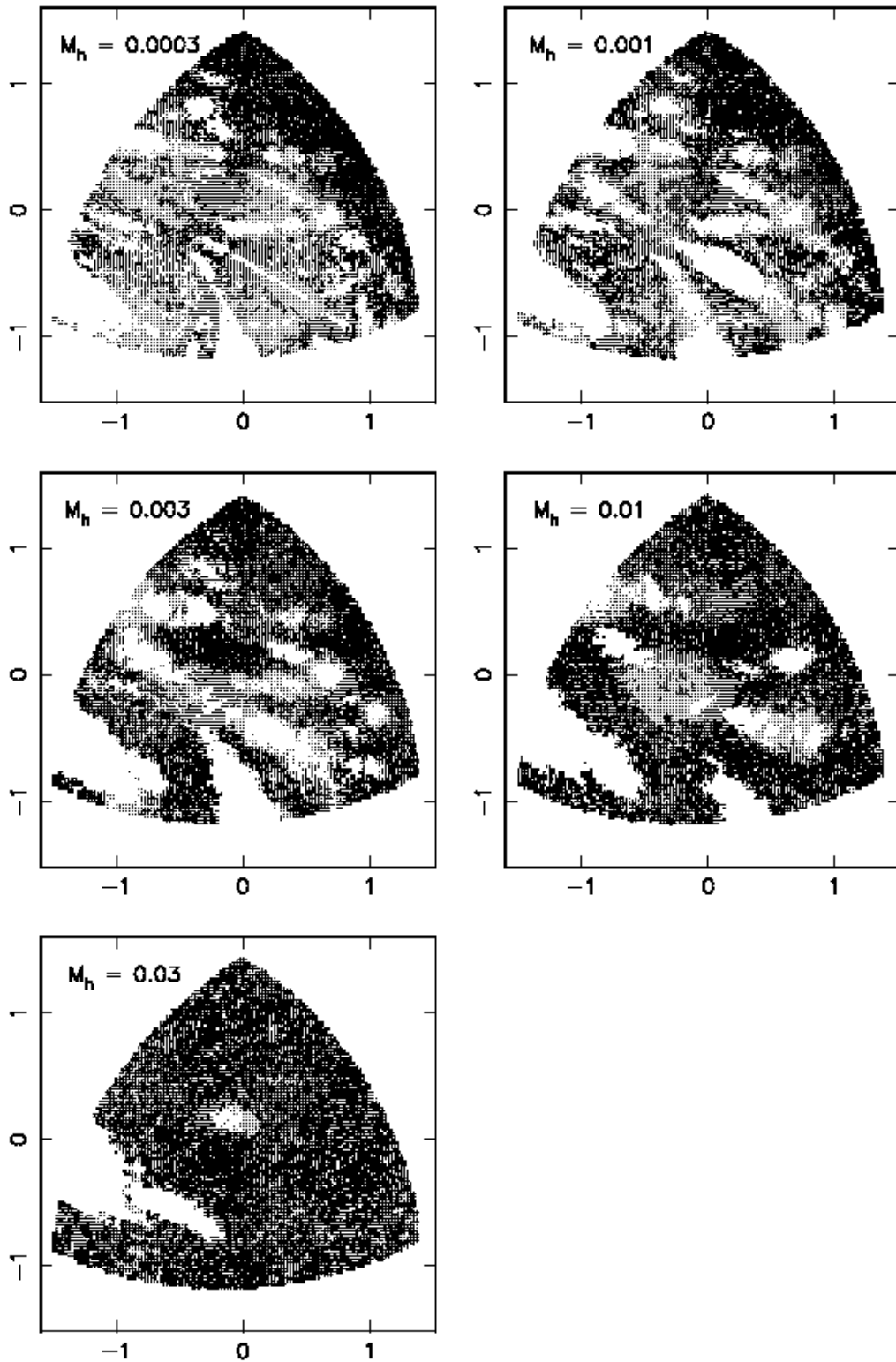


Figure 10. Initial condition space at shell 8 in a set of models with $c/a = T = \gamma = 0.5$, and various values of M_h , the mass of a central singularity. The grey scale is proportional to the logarithm of the diffusion rate in frequency space, defined as the fractional change in the largest-amplitude fundamental frequency over 50 periods of the long-axis orbit (in the model without a central point mass). White regions correspond to regular orbits.

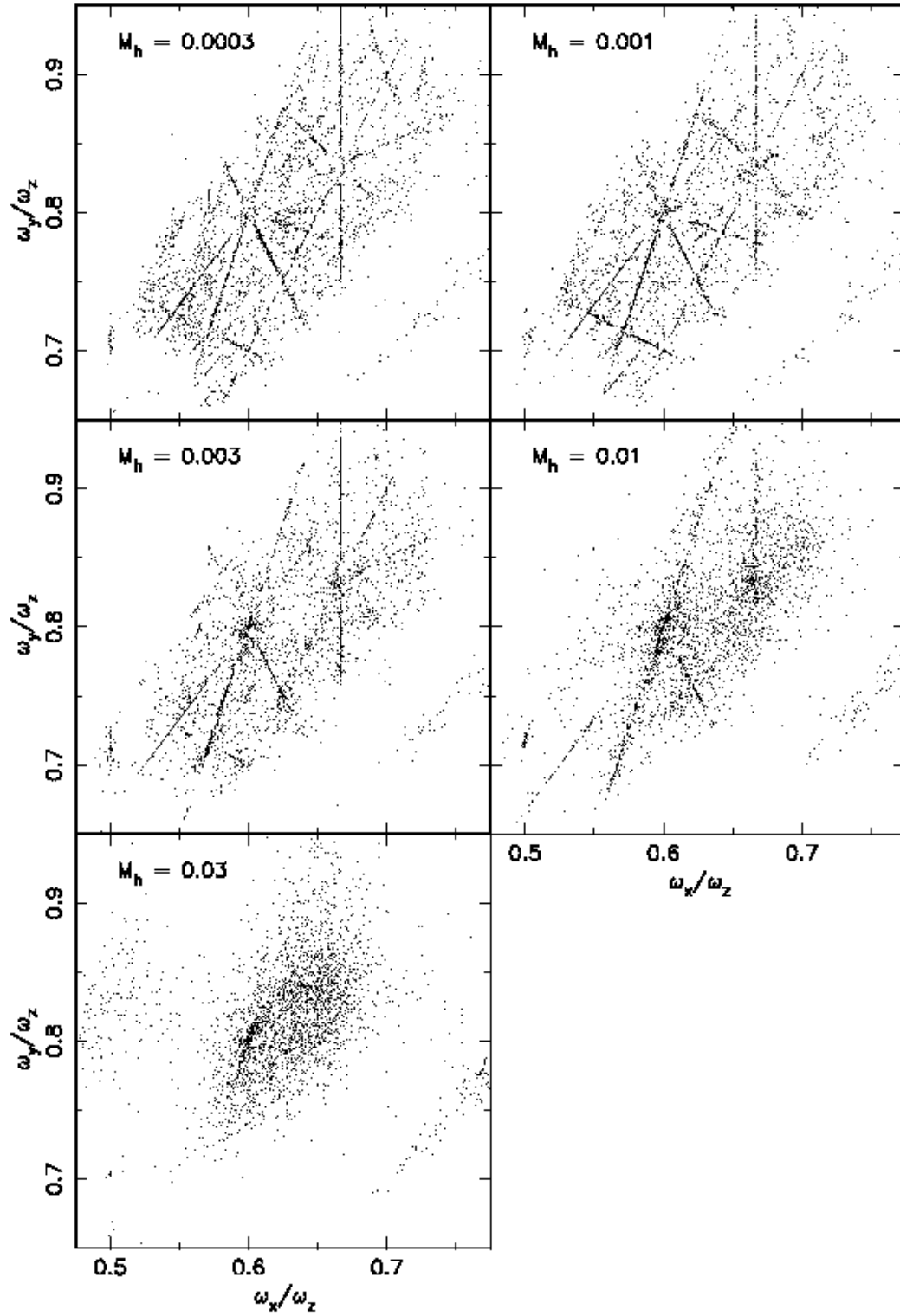


Figure 11. Frequency maps for the orbits of Figure 10.

this range (Merritt & Fridman 1995; Gebhardt et al. 1996), with the steeper cusps usually appearing in fainter galaxies. The diffusion rates have been normalized by dividing the change in ω by the frequency of the long-axis orbit in all of the models. Since the orbital integrations were carried out for a fixed number of long-axis orbital periods, the diffusion rates plotted in Figure 8 may be interpreted as the fractional change in ω that takes place over a fixed number (50) of orbital oscillations.

For $\gamma = 0$, both the diffusion plots and the frequency maps reveal that the motion is largely regular, at least over the interval of $\sim 10^2$ oscillations for which the orbits were integrated. The stochastic orbits are mostly identified with the instability strip that connects the y and z axes in initial condition space. A number of orbits that lie close in frequency space to a resonance between the three degrees of freedom exhibit weaker stochasticity; the most prominent resonance is the $(1, -2, 1)$, which extends from the $y - z$ instability strip through the unstable, $4 : 5 : 6$ and $3 : 4 : 5$ periodic orbits. However the diffusion rates for most of these orbits are lower than that in the $y - z$ instability strip by orders of magnitude. As a result, the majority of orbits outside of the $y - z$ instability strip remain in a smooth grid in the frequency map.

As γ is increased from 0 to 1, the area in initial condition space associated with resonance layers becomes larger. Almost all of the regular orbits in the $\gamma = 1$ model can be associated with a stable resonance, and a smaller number with stable periodic orbits that lie at the intersection of two or more resonances. The regions between the resonance lines in the frequency map now show almost no hint of a regular grid; in other words, essentially none of the phase space in the $\gamma = 1$ model can be usefully identified with the integrable phase space of a Stäckel potential. Nevertheless, the majority of the strongly stochastic orbits remain confined to the $y - z$ instability strip; diffusion rates in other parts of initial condition space are generally much lower.

The most dramatic change in the structure of phase space occurs as γ is increased from 1 to 2. The $y - z$ instability strip enlarges to include most of the equipotential surface; the diffusion rates in this interconnected stochastic region become nearly constant, implying that the stochastic motion is essentially free to explore the entire phase-space region accessible to it. Most of the stable resonance zones disappear, leaving finally only the $(2, 0, -1)$ and $(3, -1, -1)$ resonances with appreciable numbers of associated regular orbits. In fact a large fraction of the regular orbits in the $\gamma = 2$ model appear to be closely associated with just three, stable periodic orbits: the $1 : 2$ $x - z$ banana orbit (the $2, 0, -1$ resonance); and the $4 : 5 : 7$ and $5 : 7 : 8$ orbits (both associated with the $3, -1, -1$ resonance). Essentially all of the points on the frequency map that lie away from these two resonance lines are stochastic. However, a certain amount of structure remains in stochastic phase space, since many of the fundamental frequencies returned by the NAFF algorithm for the stochastic orbits are clustered near one or more resonance lines. In other words, over time intervals of $\sim 10^2$ oscillations, many of the stochastic orbits continue to

behave to a certain extent like regular orbits, with more-or-less well-defined frequencies.

Figures 10 and 11 present the analogous results for ensembles of orbits in models with $\gamma = 0.5$ and with five different values of M_h , the mass of a central singularity in units of the total mass of the model. The progression from essentially regular to essentially chaotic motion is now more dramatic. Even for $M_h = 0.0003$, the regular grid in the frequency map is destroyed, and the motion is dominated by the resonances. As M_h approaches 0.01, the $y - z$ instability strip enlarges to include most of the equipotential surface, and the diffusion rates are uniformly high throughout most of stochastic initial condition space. The structure in the frequency map is almost completely destroyed when $M_h = 0.03$. The only remaining regular orbits are associated with the $x - z$ banana orbit and the $3 : 4 : 5$ periodic orbit, while the stochastic orbits are distributed almost randomly around the frequency map. In terms of the definitions presented above, the phase space of the $M_h = 0.03$ model (at least, that part of phase space associated with boxlike orbits) appears to be in the globally stochastic regime. While the precise value of M_h corresponding to the transition to global stochasticity is not clearly defined, Figures 10 and 11 suggest that it lies between 0.01 and 0.03 at this energy.

By comparison, even the steepest cusp ($\gamma = 2$) appears to generate no more stochasticity than a central singularity with $M_h \approx 0.003$. In other words, in models without a central black hole, the transition to global stochasticity appears to be just beginning as γ increases above 2.

The transition to global stochasticity seen in the boxlike orbits is in sharp contrast to the behavior of the tubes. Since the time-averaged angular momenta of tube orbits is nonzero, tube orbits never go close enough to the center to experience the effects of a steeply-rising central force. Consequently, one does not expect the structure of phase space as seen in either diffusion rate plots or the frequency map (Figure 5) of tube orbits to show much dependence on cusp slope. This was in fact found to be the case. The stochasticity in the tube orbits arises from the inherent non-integrability of the model, and its character is determined by the overall shape of the potential, not by any peculiarity of the central density structure.

It was remarked above that regular orbits could be classified in terms of their degree of degeneracy, i.e. in terms of the number of independent resonance conditions $l\omega_1 + m\omega_2 + n\omega_3 = 0$ that define their associated phase-space regions. Figures 8 and 10 suggest that a systematic change takes place in the typical degree of degeneracy of the regular orbits as the strength of the perturbation is increased. In weakly chaotic potentials (e.g. $\gamma = 0$, $M_h = 0$), most of the regular orbits lie in regions of zero-fold degeneracy, i.e. strongly non-resonant regions that have retained their integrable character in spite of the perturbation of the Hamiltonian away from integrable form. As the perturbation is increased ($\gamma = 0.5$), a larger fraction of the regular orbits lie in resonance zones, regions defined by a single resonance condition. When the perturbation is large ($\gamma = 2$), the only remaining regular orbits lie in regions of two-fold degeneracy, i.e. regions associated with stable periodic orbits.

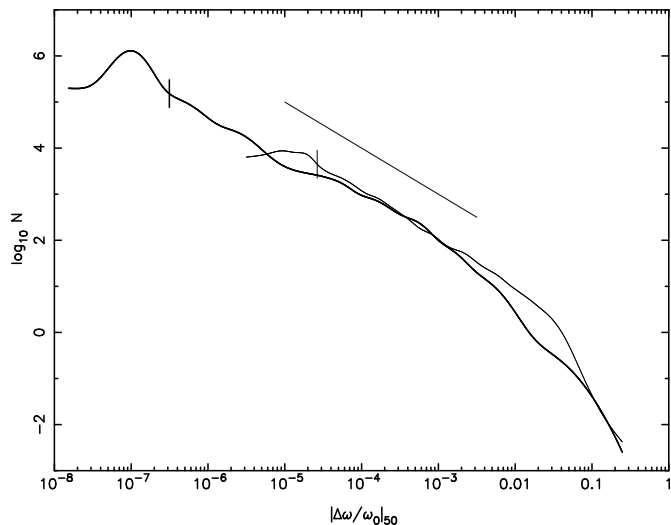


Figure 12. Spectra of diffusion rates for two ensembles of boxlike orbits at shell 8 in the model with $\gamma = 1$. The thin curve was derived from $\sim 10^4$ orbits integrated for 100 orbital periods; the thick curve is from $\sim 10^3$ orbits integrated for 400 periods. Tick marks separate regular from stochastic orbits, as discussed in the text. The thin straight line has a logarithmic slope of -1 .

5 DIFFUSION

5.1 Spectra of Diffusion Rates

While the distinction between regular and stochastic motion is unambiguous in principle, stochastic orbits can mimic regular orbits for very long times (Contopoulos 1971). This is shown clearly in Figure 12, a plot of the distribution of diffusion rates for boxlike orbits at shell 8 in the $\gamma = 1$ model. The thin curve was derived from the same $\sim 10^4$ orbits whose frequency map is displayed in Figure 9. The solid curve is from a smaller set of $\sim 10^3$ orbits integrated for a total of 400 long-axis orbital periods, four times the integration interval of the larger ensemble. (The accuracy of the numerical integration routine was increased for the longer run.) Since the precision with which the NAFF algorithm computes the fundamental frequencies is a strong function of the integration interval (Laskar 1996), we expect the solid curve to extend to smaller values of $\Delta\omega$ than the thin curve, assuming of course that very weakly chaotic orbits exist in this potential. The abscissa, $|\Delta\omega/\omega_0|_{50}$, is the change in fundamental frequencies over an interval of 50 long-axis orbital periods, normalized to ω_0 , the frequency of the long-axis orbit at shell 8. In the longer run, the measured changes in ω were scaled to the shorter interval following the procedure described in §6.

The spectrum of diffusion rates is well described as a power law in $\Delta\omega$ with logarithmic slope close to -1 . In the run with the longer integration interval (solid curve), this power law distribution extends over at least six decades in $\Delta\omega$, a remarkable range. Evidently, an appreciable fraction of the stochastic orbits in this model exhibit motion that is very nearly, though not quite, regular. This fact makes it difficult to decide which orbits are regular – there is no well-

defined break in the spectrum at low $\Delta\omega$. Presumably, many of the orbits with $\Delta\omega$ below the minimum value detectable by the NAFF routine are regular. Based on the accuracy tests described above, we estimated, for the shorter run, the smallest significant value of $\Delta\omega$. This value, indicated by the thin vertical tick mark, implies that $\sim 22\%$ of the orbits in the shorter run are effectively regular. A similar tick mark has been placed on the solid curve at the 22% point. Happily, on both curves, the tick mark falls roughly at the point where the distribution turns upward: sharply in the case of the longer run, more weakly in the case of the shorter run. Plots of the starting points on the equipotential surface of orbits to the left of the tick marks also show a very similar distribution for the two ensembles. We conclude that roughly 1/5 of the orbits in each ensemble are regular, or so weakly stochastic that we can not distinguish them from regular orbits.

One might reasonably ask whether there are *any* regular orbits in these ensembles. Perhaps the upturn at small $\Delta\omega$ in Figure 12 reflects a population of orbits with extremely low but nonzero diffusion rates. We consider such an interpretation to be unlikely. Certain of the periodic orbits in this initial condition space (e.g. the $x-z$ banana) are known to be stable to small perturbations (Fridman & Merritt 1997) and must have families of associated regular orbits. The orbits with the lowest diffusion rates do in fact have initial conditions lying close to these stable periodic orbits. A number of experiments reassured us that the upturn at small $\Delta\omega$ in the distribution of diffusion rates always occurs at roughly the same percentile point in a given initial-condition space, regardless of (modest) changes in the integration interval or accuracy of the numerical integrator. If there were no bona-fide regular orbits, we would expect to see the fraction of orbits with significantly nonzero $\Delta\omega$'s increase monotonically with increasing accuracy of the numerical routines.

In any case, we clearly see a smaller population of regular box orbits here than was seen in many earlier studies. For instance, Merritt & Fridman (1996) used Liapunov exponents to study orbits in the same $\gamma = 1$ model investigated here. In their ensemble of 192 boxlike orbits from shell 8, they estimated that $\sim 40\%$ were regular (their Figure 7a), roughly twice the fraction of regular orbits found here. This difference is not surprising given the greater sensitivity of the NAFF algorithm to weak stochasticity. Figure 12 implies that Merritt & Fridman (1996) were unable to detect stochasticity in orbits with $\Delta\omega/\omega_0$ less than about 3×10^{-4} . As we show below, such small amounts of diffusion correspond to very nearly regular behavior.

The existence of a population of stochastic orbits with very low diffusion rates is consistent with a number of studies of motion in “decomposable” phase spaces, i.e. systems containing both regular and stochastic trajectories (e.g. Karney 1983). In decomposable systems, stochastic orbits are hampered in their diffusion by invariant tori; when a large fraction of phase space is associated with such tori, many of the stochastic orbits exhibit quasi-regular behavior over long periods of time.

The approximately $1/\Delta\omega$ distribution of diffusion rates in Figure 12 can not extend to very large or very small $\Delta\omega$'s

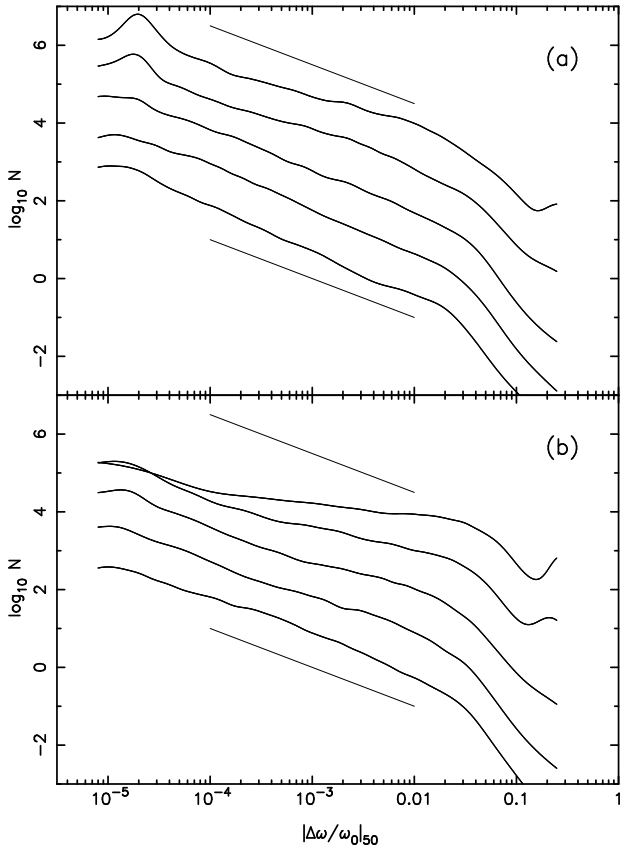


Figure 13. Spectra of diffusion rates for the ten ensembles of boxlike orbits. (a) $M_h = 0$; $\gamma = 0, 0.5, 1, 1.5, 2$, increasing upward. (b) $\gamma = 0.5$; $M_h = 0.0003, 0.001, 0.003, 0.01, 0.03$, increasing upward. The thin straight lines have power-law slopes of -1 . The curves are offset vertically with respect to each other by one unit in the ordinate.

without producing a logarithmic divergence in the total number of orbits. In the spectrum derived from the shorter run, we in fact observe a dropoff for $|\Delta\omega/\omega_0|_{50} \gtrsim 0.05$. This is expected, since the fundamental frequencies associated with orbits at a given energy are restricted to a range of values near the oscillation frequencies along the major axes, which means that $\Delta\omega/\omega_0$ can never exceed unity and will generally be much smaller. There must also be a falloff for small diffusion rates, but this apparently occurs at such small values of $\Delta\omega$ that it is obscured by the contribution from regular orbits.

Figure 13 shows the distribution of diffusion rates for the full set of 10 ensembles whose frequency maps are displayed in Figures 9 and 11. As the degree of central mass concentration is increased, the spectra become shallower, i.e. a larger fraction of the orbits are strongly diffusing. The logarithmic slope decreases from ~ -1 for $\gamma \lesssim 1$ to ~ -0.85 for $\gamma = 1.5$ and ~ -0.75 for $\gamma = 2$. There is a corresponding decrease in the fraction of regular orbits: from $\sim 32\%$ for $\gamma = 0$ to $\sim 18\%$ for $\gamma = 2$. In the models with a central point mass, the spectra are better described as two power

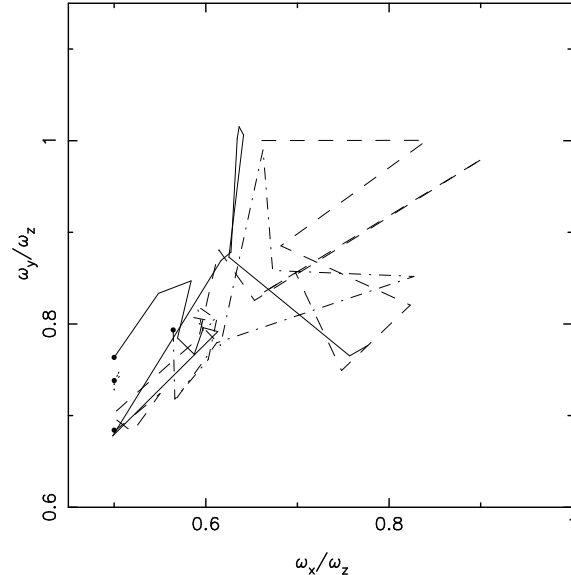


Figure 14. Diffusion in frequency space of four stochastic orbits in the model with $\gamma = 2$ and $M_h = 0$. All the orbits have similar values of $|\Delta\omega/\omega_0|_{50}$. Solid dots mark the starting points; line segments connect positions in the frequency map obtained at intervals of 50 orbital periods, for a total of 800 periods.

laws, with the shallower power law characterizing the larger diffusion rates. For $M_h = 0.001$, the shallower power law has a logarithmic slope of ~ -0.85 ($\sim 15\%$ regular), increasing to ~ -0.56 for $M_h = 0.01$ ($\sim 12\%$) and ~ -0.32 for $M_h = 0.03$ ($\sim 5\%$). We stress that our orbits are not selected in a uniform way from the energy hypersurface and the distribution of diffusion rates that we find need not be characteristic of phase space as a whole. Nevertheless the lesson of these plots seems clear: as one increases the central mass concentration of a triaxial model, the fraction of regular orbits drops and the typical diffusion rate goes up.

5.2 The Character of Diffusion in Frequency Space

As a stochastic orbit evolves, it visits different parts of frequency space, eventually moving far away from its initial location. In Figure 14 we plot the trajectory in frequency space of four orbits in the $\gamma = 2$ model. The solid dot in each curve marks the initial location of the orbit; successive positions in frequency space, at intervals of 50 orbital periods, are joined by line segments. For three of the orbits, the motion in frequency space is reminiscent of a random walk, in the sense that successive displacements are not strongly correlated. The fourth orbit appears to diffuse far less than the other three. A comparison with the frequency map of Figure 9 shows that this orbit is located close to the $x-z$ banana and is evidently trapped in the associated resonance layer.

Assuming a random walk in frequency space, the distance that an orbit moves from its starting point should increase approximately as $t^{1/2}$, with t the elapsed time. In

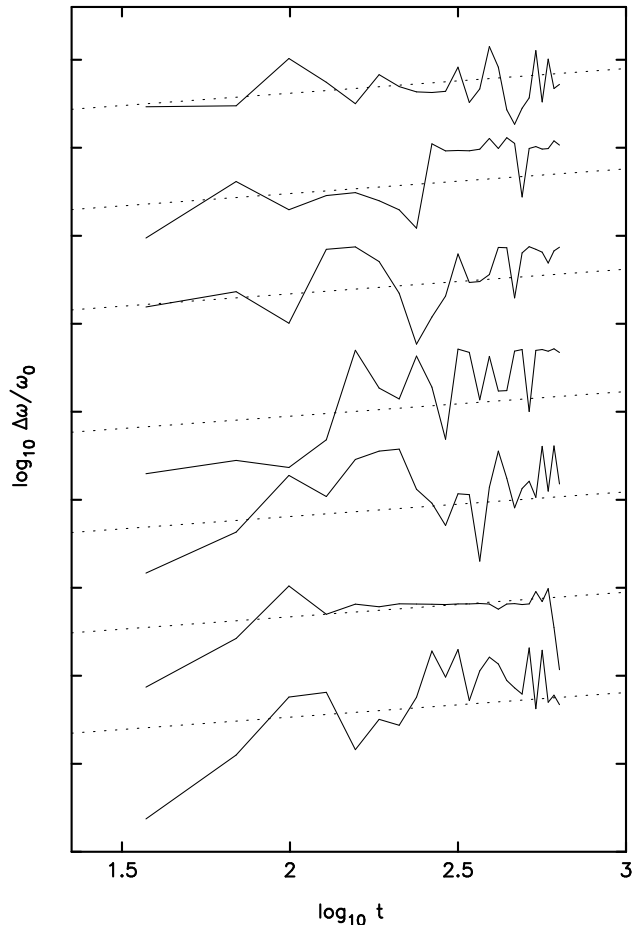


Figure 15. Cumulative change in fundamental frequencies versus time for seven stochastic orbits. The straight lines have logarithmic slopes of 0.5.

Figure 15 we show the time evolution of $\Delta\omega$ (as defined above) for 7 different orbits from the model with $\gamma = 0.5$ and $M_h = 0.03$. These 7 orbits are representative of a larger sample of 100 that were randomly selected from the large ensemble of 10^4 orbits discussed previously, on the basis that their diffusion over 50 orbital periods satisfied $1 \times 10^{-4} \leq |\Delta\omega|/\omega_0 \leq 3 \times 10^{-4}$. The dotted line has a logarithmic slope of 1/2. While there are large excursions in the value of $\Delta\omega$ for each of the orbits, there is a reasonably clear trend for $\Delta\omega$ to increase monotonically with time with an approximately $t^{1/2}$ dependence. For orbits with initially larger values of $\Delta\omega/\omega_0$, the diffusion was found to saturate rapidly, as expected given that frequency space at a given energy is bounded.

While it is beyond the scope of this paper to investigate the character of stochastic diffusion in more detail, a limited number of experiments convinced us that the diffusion of boxlike orbits in moderately stochastic potentials – corresponding to models with $\gamma \gtrsim 1$ or $M_h \gtrsim 0.003$ – can often be approximated as a random walk. We will make use of this result in the following section.

5.3 The Consequences of Diffusion for the Shapes of Orbits

Orbits that diffuse very slowly through frequency space are effectively regular: they maintain a well-defined shape for long periods of time. Stochastic orbits are significant from the standpoint of galaxy evolution only if the configuration-space volume through which they move changes substantially over the time period of interest. We therefore need to ask how large a value of $\Delta\omega/\omega_0$ corresponds to a significant change in the configuration-space volume filled by an orbit. To answer this question, we selected sets of orbits from the $\gamma = 2$ ensemble having a wide range of $\Delta\omega$'s, but lying within small patches on the equipotential surface. Orbits which originate in a small region would be expected to have similar shapes if not for the fact that they were stochastic. By comparing orbits within such a set, we can estimate how much change in configuration space density is implied by a given value of $\Delta\omega$.

The orbits were integrated for 50 periods and their configuration-space trajectories recorded. Figure 16 presents a selection of orbits taken from five different patches on the equipotential surface. Region 1 lies near the starting point of the x -axis orbit, while region 5 lies above the $x - y$ plane roughly halfway between the x and y axes. In a fully integrable potential, these starting points would all be associated with narrow box orbits, orbits that are elongated in the same sense as the figure. Narrow box orbits are often found to be heavily populated in self-consistent triaxial models (Schwarzschild 1979) and any significant evolution in their shapes would be expected to have important consequences for a triaxial galaxy.

Figure 16 shows that the degree of orbital evolution is crudely predictable given the change in fundamental frequencies. For $\Delta\omega/\omega_0 \approx 10^{-4}$, the orbits are almost indistinguishable from regular orbits, accurately maintaining their elongated shapes. For $\Delta\omega/\omega_0 \approx 10^{-3}$, the orbits are noticeably irregular, and for $\Delta\omega/\omega_0 \approx 10^{-1}$ the orbits have almost entirely lost their elongated characters. From these experiments, we estimate that a fractional change in fundamental frequencies of order $\Delta\omega/\omega_0 \approx 0.03$ corresponds to a significant change in the configuration-space shape of an orbit. If a large fraction of the boxlike orbits in a triaxial model experienced changes of this order over some specified length of time, we might expect the model to evolve strongly in shape over the same interval.

Figure 17 shows how the fraction F of orbits with $|\Delta\omega/\omega_0|_{50}$ exceeding some fiducial value varies with γ and M_h in the ensembles of Figure 9. In models without a black hole, a modest fraction of the boxlike orbits, $F \approx 20\%$, have evolved strongly after 50 orbital periods when the cusp is steep, $\gamma \approx 2$. In the models with a black hole, the fraction of boxlike orbits with $|\Delta\omega/\omega_0|_{50} > 0.03$ reaches $\sim 50\%$ for $M_h = 0.03$, and exceeds 20% for all $M_h \gtrsim 0.01$. Fully 75% of the boxlike orbits – i.e., essentially all of the stochastic boxlike orbits – have $|\Delta\omega/\omega_0|_{50} > 0.01$ in the $M_h = 0.03$ model, as expected if this initial-condition space is in the globally-stochastic regime.

We discuss in more detail below how one might trans-

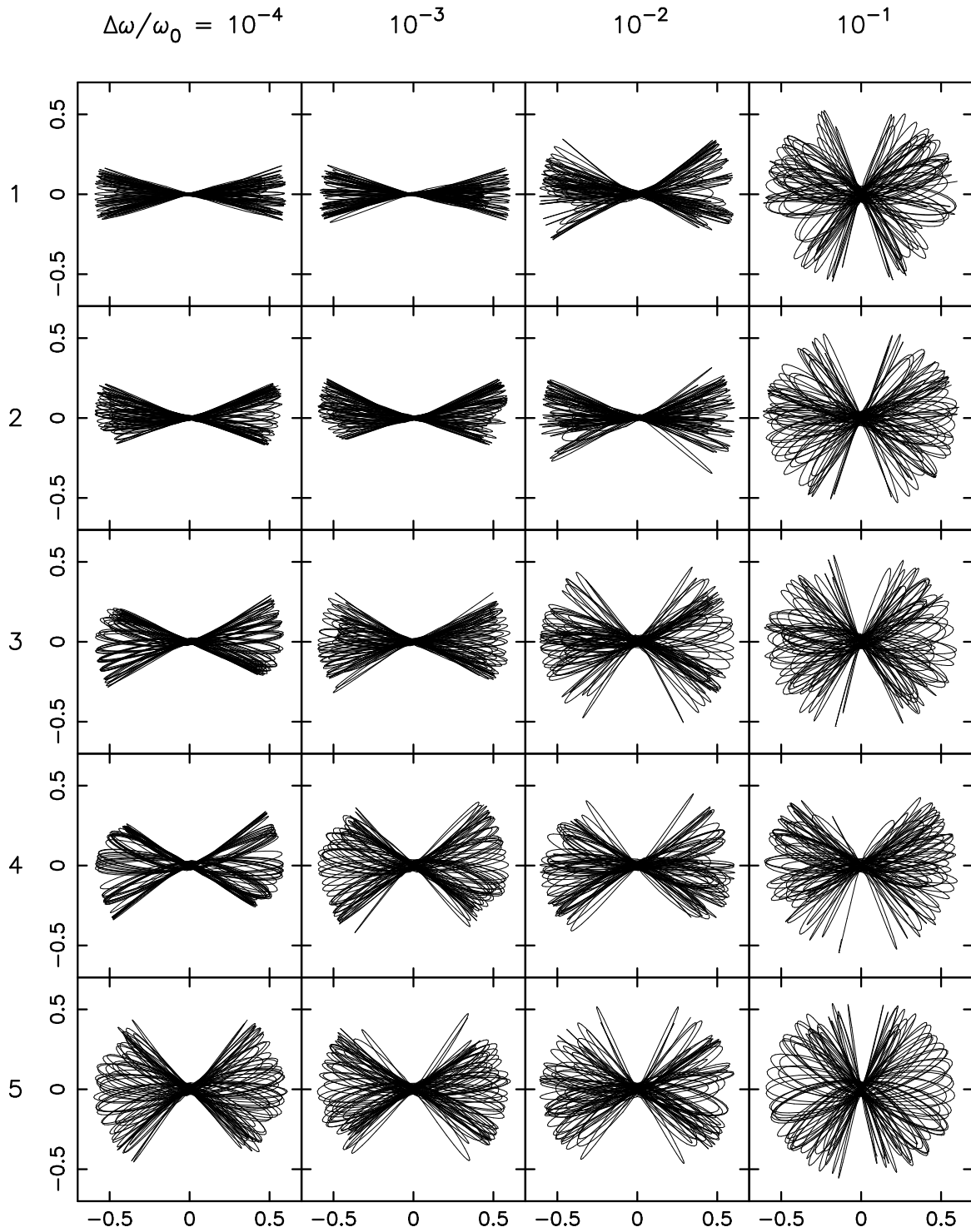


Figure 16. Boxlike orbits from shell 8 of the model with $\gamma = 2$, integrated for 50 orbital periods. The abscissa and ordinate are the x and y axes in each plot. Initial conditions were drawn from one of five small patches on the equipotential surface, as described in the text and labelled at the left. In each column, orbits were chosen to have similar values of $\Delta\omega/\omega_0$, as indicated at the top.

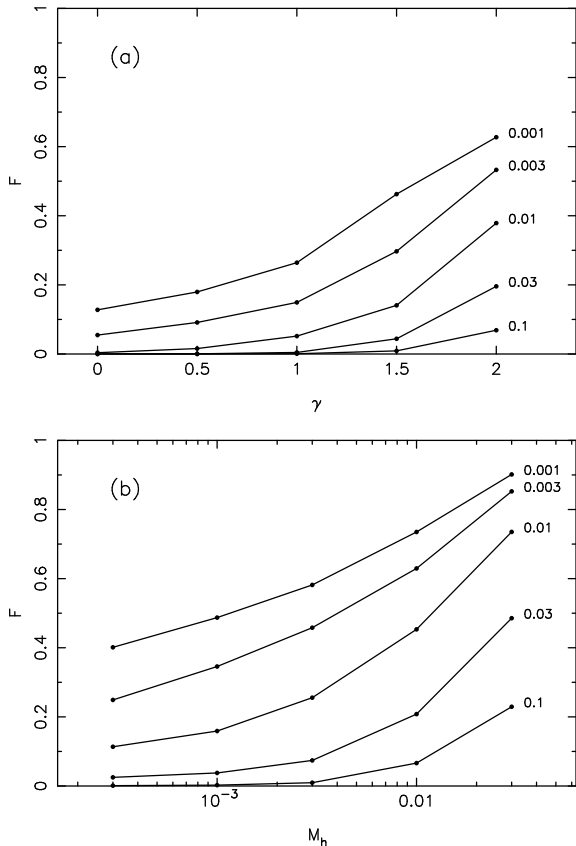


Figure 17. Fraction of boxlike orbits at shell 8 with $|\Delta\omega/\omega_0|_{50}$ exceeding some fiducial value, as indicated on the right. (a) $M_h = 0$; (b) $\gamma = 0.5$.

late these numbers into rough estimates of the time over which a triaxial galaxy would evolve in shape. However, a few conclusions follow unambiguously from Figure 17. Even a relatively modest black hole, $M_h \approx 0.003$, induces about as much stochastic diffusion in the boxlike orbits as does a steep central cusp, $\gamma = 2$. Since the average ratio of black hole mass to galaxy mass is believed to be about 0.005 (Kormendy & Richstone 1995), Figure 17 suggests that the chaotic evolution in most early-type galaxies will be driven more by the central black hole than by the stellar cusp.

The greater effectiveness of black holes compared with cusps at inducing chaos is not surprising. Miralda-Escudé & Schwarzschild (1989) point out that the gravitational force from even a steep density cusp, $\rho \propto r^{-2}$, fails to produce the large-angle deflections that result from close passage to a point mass.

5.4 Dependence of Diffusion Rates on other Parameters

Up till now, all of our results were derived from orbits at shell 8, whose apocenters lie just inside the half-mass radius of the model. Furthermore we have only discussed a single,

relatively elongated mass model, with $c/a = 0.5$. Most elliptical galaxies are less elongated than this (Tremblay & Merritt 1995). Here we extend our results to a range of different energies in models with two additional shapes: $c/a = 0.6$ and 0.8 . We continue to assume “maximal triaxiality.” In each model, we carried out a frequency analysis of ~ 500 boxlike orbits at each of five energies, corresponding to shells 3, 6, 9, 12 and 15. As before, we considered five different values of the cusp slope γ and five different values of the black hole mass M_h (the latter in models with $\gamma = 0.5$). Orbits were integrated for 50 periods of the long-axis orbit at the energy corresponding to their shell.

In the models without a central black hole, the spectrum of diffusion rates was found to vary only modestly from shell to shell. In other words, boxlike orbits experience roughly the same degree of evolution, after a fixed number of orbital periods, at all energies. (Since orbital periods are shorter near the center of every model, this result implies a *greater* degree of evolution at low energies after a fixed interval of time.) The greatest dependence on energy was seen in models with a weak cusp, $\gamma \approx 0$; these models have nearly-harmonic cores and the stochasticity becomes less important at low energies. In models with $\gamma \gtrsim 1$, almost no variation with energy is seen (Figure 18).

In models with a central black hole, there is a stronger dependence of diffusion rates on energy (Figure 19). At low energies, an increasingly large fraction of the boxlike orbits exhibit strong diffusion over a fixed number of orbital periods. This is reasonable, since at low energies the black hole contains a large fraction of the interior mass.

Figures 18 and 19 also indicate a modest dependence of diffusion rates on galaxy elongation c/a . However, this dependence is likely to be swamped by the fact that the boxlike orbits occupy a rapidly decreasing fraction of phase space in more axisymmetric potentials.

One might expect the critical value of M_h for transition to global stochasticity (§4) to depend on c/a and on energy. If we define a globally-stochastic initial-condition space as one in which 5% or less of the boxlike orbits are regular – roughly the fraction at shell 8 in the model with $M_h = 0.03$ (Figure 10) – we find that the transition takes place at shell 3 when $M_h \approx 0.005$, at shell 6 when $M_h \approx 0.01$, at shell 9 when $M_h \approx 0.02$ and at shell 12 when $M_h \approx 0.03$ in the model with $c/a = 0.6$. When $c/a = 0.8$, we find $M_h \approx 0.002$ at shell 3, ~ 0.004 at shell 6, ~ 0.01 at shell 9 and ~ 0.02 at shell 12.

We note that diffusion rates of stochastic orbits in real galaxies might depend on additional factors not considered here, such as the discreteness of the potential or its dependence on time. For instance, Habib, Kandrup & Mahon (1997) have argued that even very small amounts of additive noise can greatly enhance the diffusion rate in 2 DOF systems. We hope to address this issue in a subsequent paper.

6 EVOLUTION

Diffusion of stochastic orbits is an irreversible process. Because chaotic motion is essentially random over long time

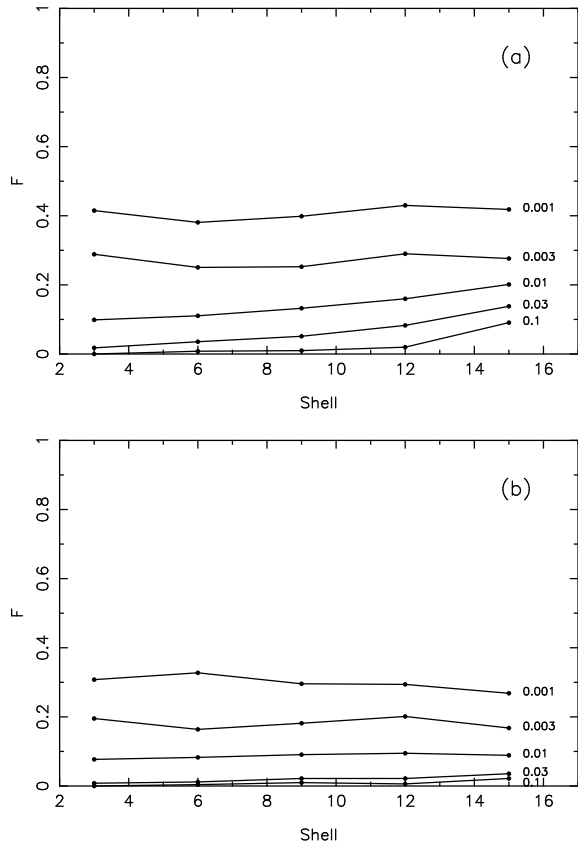


Figure 18. Fraction of boxlike orbits with $|\Delta\omega/\omega_0|_{50}$ exceeding some fiducial value, as a function of shell number, for $\gamma = 1.5$ and $M_h = 0$. (a) $c/a = 0.6$; (b) $c/a = 0.8$.

intervals, the probability of finding a single star anywhere in stochastic phase space tends toward a constant value at all accessible points; in other words, the density of an ensemble of stars in stochastic phase space evolves toward a constant, coarse-grained value. Something similar to this takes place in regular phase space as stars on nearby orbits gradually move out of phase. But chaotic mixing is more efficient than phase mixing because the region accessible to a stochastic orbit is much larger than the single torus to which a regular orbit is confined, and because the divergence between adjacent stochastic trajectories grows exponentially at early times (Kandrup & Mahon 1994; Merritt & Valluri 1996). In a fully mixed galaxy, there is only one “orbit” or “invariant density” at each energy in stochastic phase space, and this orbit has a configuration-space shape that is poorly suited to reproducing the shape of the galaxy (Merritt & Fridman 1996). If diffusion times for a significant fraction of the orbits in a triaxial galaxy are short compared to the galaxy’s lifetime, the galaxy would be expected to evolve toward more spherical or axisymmetric shapes as the stochastic parts of phase space approach a fully mixed state.

We wish to estimate the approximate rate of this evolution. In particular, we want to know how the rate of

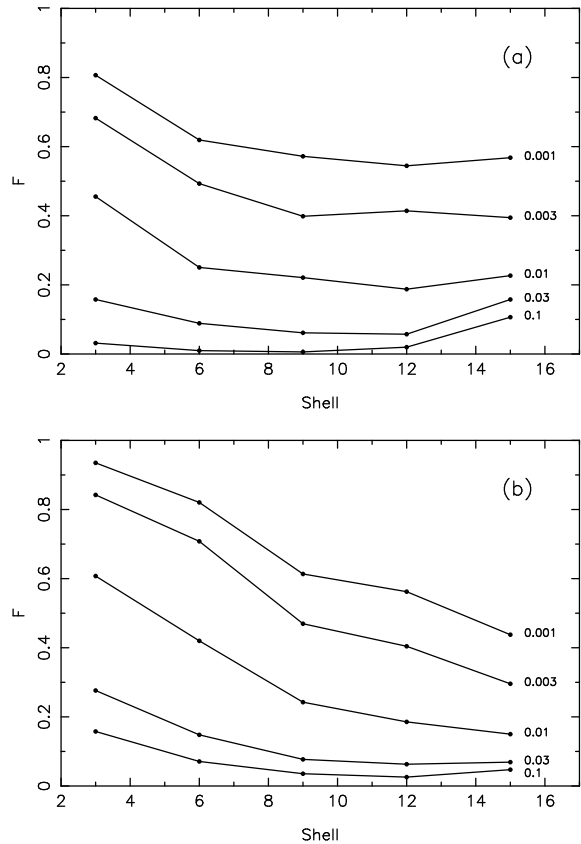


Figure 19. Fraction of boxlike orbits with $|\Delta\omega/\omega_0|_{50}$ exceeding some fiducial value, as a function of shell number, for $M_h = 0.003$ and $\gamma = 0.5$. (a) $c/a = 0.6$; (b) $c/a = 0.8$.

chaos-driven evolution varies with galaxy parameters. From a dynamical point of view, early-type galaxies comprise a two-parameter sequence, the so-called Fundamental Plane (Pahre, Djorgovski & Carvalho 1995). But to a first approximation the structural parameters of early-type galaxies can be expressed as a function of just one variable, the total luminosity. Bright elliptical galaxies and bulges have lower average densities, larger characteristic radii and shallower central density cusps than faint ellipticals. These trends imply that chaotic mixing should be most effective in faint (triaxial) galaxies, for at least two reasons. First, crossing times are shortest in faint ellipticals, and stochastic diffusion rates scale approximately with orbital frequency. Second, faint ellipticals have higher central concentrations, implying a greater degree of stochastic evolution for boxlike orbits after a given number of orbital periods. Bright ellipticals might also be dynamically younger than faint ellipticals in the sense of having formed more recently via mergers. We will argue below that the greater effectiveness of chaotic mixing in fainter ellipticals may be responsible for many of the systematic differences between them and bright ellipticals, including their lower degree of triaxiality and their less boxy isophotal shapes.

In this section, we use the diffusion-rate calculations of §5 to estimate how great a degree of orbital evolution would be expected after a Hubble time in real elliptical galaxies. We begin (§6.1) by using observational data to estimate the average dependence of galaxy crossing time on luminosity, which allows us to determine how the “dynamical ages” of ellipticals vary with their absolute magnitude. Since our calculations in §5 yielded spectra of diffusion rates after a fixed interval of 50 orbital periods, we need to find a way to scale those spectra to different elapsed times. We do this (§6.2) by assuming that diffusion in frequency space can be approximated as a random walk. We can then calculate the fraction of boxlike orbits that would have experienced substantial evolution over a galaxy lifetime as a function of galaxy luminosity.

Evolution of individual orbits is significant only if phase space is populated in a non-uniform way to start with; in a fully mixed galaxy, stochastic diffusion would leave the phase space density unchanged, i.e. constant in each disjoint region. Our assumption throughout this section is that galaxies form in a state that is not fully mixed, and hence that diffusion of stochastic orbits can lead to a change in a galaxy’s shape. We clearly do not have access here to the tools that would be required to accurately calculate the rate of such change; at a minimum, we would need to know the orbital population of a self-consistent model before we could convert our orbital diffusion rates into rates of change of the self-consistent shape. Nevertheless we can make some tentative statements about the expected rate of evolution by comparing our results to a recent set of N -body simulations of triaxial galaxies with central black holes (§6.3).

6.1 Dependence of Elliptical Galaxy Structural Parameters on Luminosity

The observed variation of effective radius r_e with blue absolute magnitude M_B is shown in Figure 20 for a sample of 337 early-type galaxies, from the data of Jørgensen et al. (1995, 1996). The fitted line has

$$M_B = -18.440 - 3.327 \log r_e; \quad (14)$$

the slope in Equation (14) is the geometric mean of the slopes obtained by least-squares fits to M_B vs r_e and r_e vs M_B . The mean relation can be written

$$r_e \approx 12.50 \left(\frac{L_B}{10^{11} L_\odot} \right)^{0.751} \text{ kpc} \quad (15)$$

with L_B and L_\odot the blue luminosities of the galaxy and the sun, respectively. In the γ -models, the effective radius remains an approximately fixed multiple of the half-mass radius as γ is varied, $r_e \approx 0.75 r_{1/2}$ (Dehnen 1993), which allows us to replace r_e with $r_{1/2}$ in equation (15).

For the dependence of mass-to-light ratio on luminosity, we take

$$\frac{M}{L_B} = 15.3 \left(\frac{L_B}{10^{11} L_\odot} \right)^{0.25} \quad (16)$$

in solar units (Faber et al. 1987), or

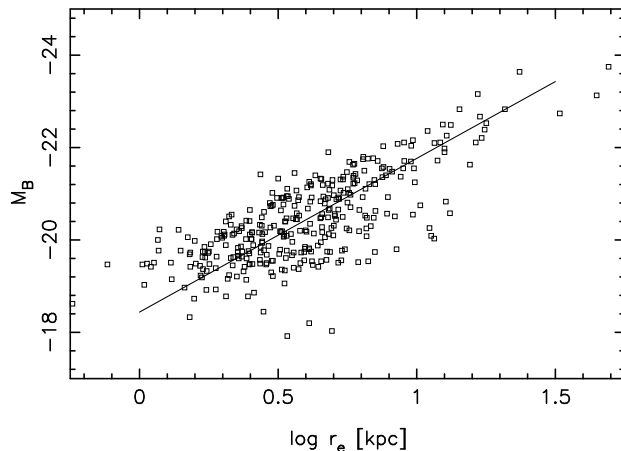


Figure 20. Relation between absolute blue magnitude and effective radius for a sample of 337 nearby E and S0 galaxies, from the data of Jørgensen et al. (1995, 1996). The line is a least-squares fit, as described in the text.

$$\frac{M}{M_\odot} = 1.53 \times 10^{12} \left(\frac{L_B}{10^{11} L_\odot} \right)^{1.25}. \quad (17)$$

The $M/L \sim L^{1/4}$ dependence of equation (16) could also have been arrived at by combining equation (15) with the virial theorem and the Faber-Jackson law.

If we define $T_{1/2}$ as the period of a circular orbit in Dehnen’s spherical model at the radius containing one-half of the total mass, equations (15) and (17) give

$$T_{1/2} \approx 2.30 \times 10^8 \left(\frac{L_B}{10^{11} L_\odot} \right)^{0.50} \text{ yr}, \quad (18)$$

independent of γ . This relation implies a modest dependence of galaxy crossing time on absolute magnitude. For $M_B = -21$, $T_{1/2} \approx 1.4 \times 10^8$ yr, or ~ 35 orbital periods after a lifetime of 5×10^9 yr. For $M_B = -18$, $T_{1/2} \approx 3.47 \times 10^7$ yr, for a dynamical age of ~ 150 periods. Finally, we can express $T_{1/2}$ in terms of the period of the axial orbit at shell 8 in our models, the unit of time in which results were presented above.

6.2 Scaling of $\Delta\omega$ to Different Time Intervals

The integration interval on which Figures 13 and 17 are based corresponds roughly to the lifetime, at the effective radius, of a bright elliptical galaxy. The orbital periods in fainter ellipticals are generally shorter. In order to draw conclusions about the degree of evolution to be expected in galaxies with a range of properties, we need to scale our results on stochastic diffusion to different intervals of elapsed time.

The experiments in §5.2 suggest that diffusion in frequency space can be reasonably approximated as a random walk over limited periods of time. Define $x = |\Delta\omega/\omega_0|_{50}$,

the fractional change in fundamental frequencies of a single orbit as computed over a time interval of t_{50} , equal to 50 orbital periods at shell 8. The spectra of diffusion rates plotted in Figure 13 are plots of $N(x)$. Assuming a random walk, the displacement of an orbit from its initial position in frequency space increases approximately as $t^{1/2}$. After some time interval $t > t_{50}$, one expects to find

$$\frac{\Delta\omega}{\omega_0} \approx x \left(\frac{t}{t_{50}} \right)^{1/2}. \quad (19)$$

Equation (19) – which is only intended to be correct in a statistical sense – allows us to estimate the change in fundamental frequencies $\Delta\omega$ after an elapsed time t given a measured $|\Delta\omega|_{50} = x\omega_0$. For $\Delta\omega/\omega_0 \approx 1$, equation (19) must break down, as discussed above; indeed, the NAFF estimate of the fundamental frequencies is only meaningful if the change in the ω 's over the integration interval is fractionally small (Laskar 1993).

Let $\Delta\omega_c$ be the change in fundamental frequencies corresponding to a substantial evolution in the configuration-space shape of an orbit. It was argued above (see the discussion accompanying Figure 16) that $\Delta\omega_c \approx 0.03\omega_0$. After an elapsed time t , the fraction F of orbits with $\Delta\omega > \Delta\omega_c$ is the fraction from the original spectrum $N(x)$ which satisfy

$$x > \frac{\Delta\omega_c}{\omega_0} \left(\frac{t}{t_{50}} \right)^{-1/2}. \quad (20)$$

Our few experiments using NAFF with different integration intervals produced results that were consistent with equation (20), though we can hardly claim to have confirmed this equation in any very general way. Equation (20) – which was used to scale the two spectra in Figure 12 – allows us to compute the spectrum of $\Delta\omega$'s after any elapsed time given a measured spectrum $N(x)$.

In the case of a $1/\Delta\omega$ distribution of diffusion rates between some limiting values x_1 and x_2 , equation (20) implies

$$F(t) \approx 1 - \log \left[\frac{\Delta\omega_c}{\omega_0} \frac{1}{x_1} \left(\frac{t_{50}}{t} \right)^{1/2} \right] / \log \left(\frac{x_2}{x_1} \right), \quad (21)$$

i.e. the fraction of strongly-evolved orbits increases logarithmically with time until $t \approx (\Delta\omega_c/\omega_0 x_1)^2 t_{50}$, at which point the phase-space distribution is “fully mixed.” This predicted behavior is consistent with what has been observed in a few earlier studies. For instance, Merritt & Valluri (1996) computed Liapunov exponents for boxlike orbits in a family of triaxial models and found that the fraction of orbits judged “stochastic” – i.e., orbits having significantly nonzero Liapunov exponents – gradually continued to increase as the integration interval was lengthened. At the half-mass energy in their model with $m_0 = 0.001$, which has a nearly r^{-2} density cusp, Merritt & Valluri found that $\sim 65\%$ of the orbits were “stochastic” over an integration interval of 10^2 periods; $\sim 72\%$ over 10^3 periods; and $\sim 79\%$ over 10^4 periods. Thus, the number of orbits behaving chaotically increased by roughly a constant amount following each factor of ten increase in the integration time, roughly as expected for a $\sim 1/\Delta\omega$ distribution of diffusion rates.

In Figure 21, equation (20) has been used to estimate the fraction of strongly-evolved orbits (orbits with

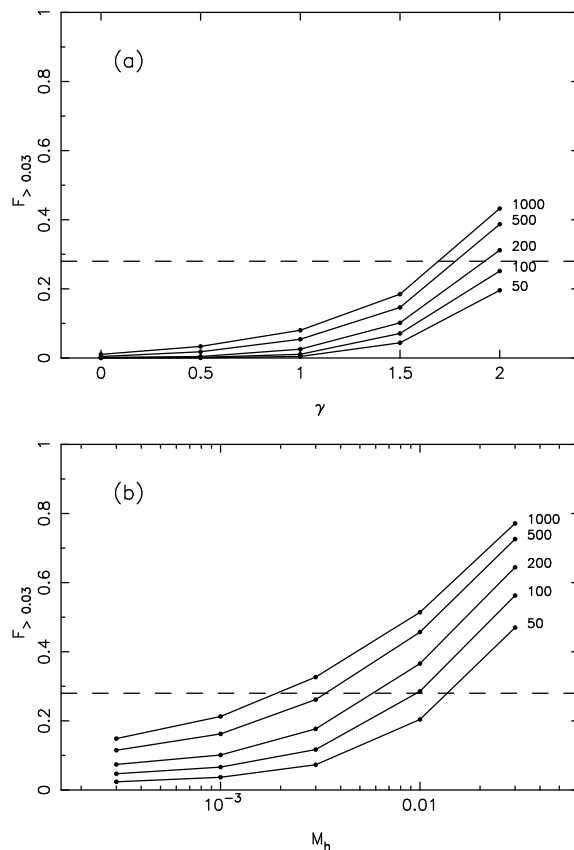


Figure 21. Fraction of boxlike orbits at shell 8 with $\Delta\omega/\omega_0$ exceeding 0.03 after some elapsed number of orbital periods at shell 8, as indicated on the right. The horizontal dashed line at $F = 0.28$ is discussed in the text.

$\Delta\omega/\omega_0 > 0.03$) as a function of elapsed time for the 10 ensembles at shell 8. In the models without a black hole, large F 's require both $\gamma \approx 2$ and elapsed times in excess of ~ 100 orbital periods. These conditions are satisfied by many low-luminosity ellipticals, which tend to have both steep cusps (Gebhardt et al. 1996) and dynamical ages in excess of 10^2 periods (equation 18). However as γ drops, Figure 21a suggests that the time required to produce a significant number of strongly-evolved orbits quickly exceeds a Hubble time. For instance, at $\gamma = 1$, a time in excess of 10^3 orbital periods is indicated, which is much longer than the typical lifetimes of the (bright) ellipticals that have weak density cusps. These results confirm earlier suggestions (Tremblay & Merritt 1996; Merritt & Valluri 1996) that the importance of stochastic diffusion in elliptical galaxies without central black holes should fall off rapidly with increasing luminosity. On the other hand, the assumption made in a number of recent self-consistency studies (Schwarzschild 1993; Merritt & Fridman 1996; Merritt 1997) of a high degree of chaotic mixing in triaxial galaxies with steep cusps, is verified by Figure 21a.

In triaxial galaxies containing a central black hole, Fig-

ure 21b suggests that F would exceed $\sim 20\%$ after 100 orbital periods for any $M_h/M_g \gtrsim 0.005$. This is roughly the black-hole mass fraction that is believed to be characteristic of early-type galaxies of all luminosities (Kormendy & Richstone 1995; Magorrian et al. 1998); among galaxies with well-determined black hole masses, galaxies as faint as M32 and as bright as M87 have $M_h/M_g \approx 0.5\%$ (van der Marel et al. 1997; Macchetto et al. 1997). As noted above, even modest black holes, $M_h/M_g \gtrsim 0.003$, are as effective as the steepest density cusps at producing stochastic diffusion. We would therefore expect the degree of dynamical evolution in real triaxial galaxies to be determined more by the mass of the central black hole than by the slope of the central density cusp. In the galaxies with the largest observed values of M_h/M_g , $M_h/M_g \approx 0.02$, Figure 21b suggests very short timescales for evolution, less than 50 orbital periods. This is as expected given the globally-stochastic nature of the phase space when M_h/M_g is so large (§4).

6.3 Comparison with N -Body Evolution

Having estimated the degree of orbital evolution to be expected in triaxial models with a range of structural parameters and ages, we would like to go one step further and ask what the consequences of this diffusion would be for evolution of a galaxy's shape. This is clearly a difficult question which can only be properly addressed through a combination of self-consistency and N -body studies. We will nevertheless attempt to calibrate the expected evolution rate against the N -body integrations of Merritt & Quinlan (1998), who followed the evolution of a triaxial galaxy in which central black holes of various masses were grown. Their initial model was strongly triaxial and had $c/a \approx 0.6$, similar to the models considered here. Merritt & Quinlan (1998) observed a nearly complete evolution to axisymmetry over ~ 40 half-mass orbital periods (defined as the period of the circular orbit at the half-mass radius in the spherically symmetrized model) when the final black hole mass was 1% of the galaxy mass. When M_h was reduced to $\sim 0.3\%$, the evolution toward axisymmetry (a state that was not quite reached at the end of the integration) proceeded at a rate 4-5 times slower. When M_h was increased to $\sim 3\%$, axisymmetry was reached in little more than a crossing time.

We can draw some immediate conclusions about the approximate dependence of evolution rates on luminosity from this N -body work. Assume, as argued by Magorrian et al. (1998), that the average ratio of black hole mass to bulge mass is roughly 0.5%, independent of bulge luminosity. Merritt & Quinlan's results suggest that a triaxial galaxy containing a black hole of this mass would evolve strongly in shape in ~ 100 periods of the half-mass circular orbit. According to equation (18), the half-mass orbital period in an elliptical galaxy equals 1% of a galaxy lifetime (of 5×10^9 years, say) when $M_B \approx -19$. Hence we would expect to see strong evolution in the shapes of triaxial galaxies fainter than $M_B \approx -19$.

This result is presented graphically in Figure 22. The ordinate in that figure is the evolution time as derived by Merritt & Quinlan (1998) for black hole masses of 0.003, 0.01

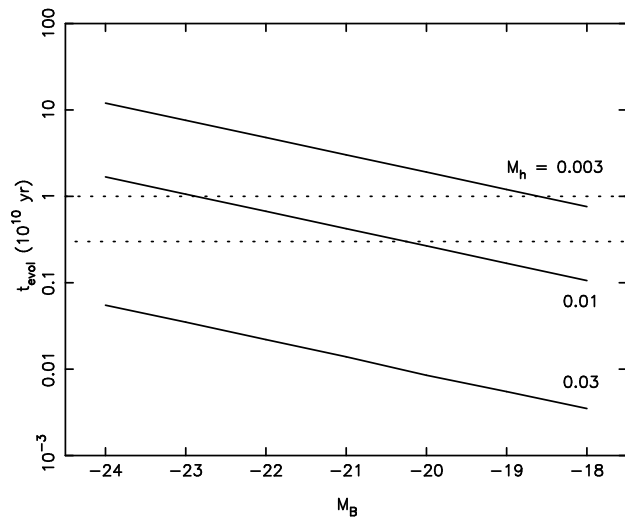


Figure 22. Estimated time for strong evolution in the shape of a triaxial galaxy as a function of absolute blue magnitude, for various black hole masses. Dashed lines bracket the expected lifetimes of elliptical galaxies.

and $0.03M_g$; evolution times have been converted to years using the scaling relation (18). The dashed lines bracket the range of reasonable galaxy lifetimes, from 3 to 10 billion years. As just argued, the critical luminosity at which t_{evol} equals the expected lifetime of a galaxy is $M_B \approx -19$ for fractional black hole masses of 0.5%. However Figure 22 suggests a rather steep dependence of this luminosity on M_h/M_g , a result of the strong dependence found by Merritt & Quinlan of galaxy evolution rates on black hole masses. Since there is considerable variation in M_h/M_g in real galaxies (Kormendy & Richstone 1995), we would expect that any black-hole-induced correlation of galaxy shape with luminosity should exhibit much scatter. As we discuss below, both the shapes of elliptical galaxies, as well as some properties that are believed to correlate with shapes, do in fact appear to undergo a change (in the correct sense) at $M_B \approx -19$ to -20 .

We would like to take this argument one further step and estimate the evolution time as a function of the full range of parameters ($\gamma, M_h/M_g$) that were considered in the orbital studies presented above. We will assume simply that significant evolution occurs when some fixed fraction F_{crit} of the stochastic orbits have evolved strongly in the sense defined in §5. Based on Merritt & Quinlan's results for $M_h = 0.01$, and scaling their time units to the units of Figure 21 (the scaling factor is 2.3), we find $F_{crit} \approx 0.28$. If we assume that the same value of F_{crit} can be used to predict the evolution toward axisymmetry in models with different black hole masses – probably only a crude approximation – then Figure 21 implies an evolution time of $\sim 250T_{1/2}$ for $M_h = 0.003$, in reasonable agreement with the rate of evolution found by Merritt & Quinlan (1998). Given this modest success, we feel justified in drawing a dashed line in Figure 22 at $F = 0.28$ and inferring evolution times for models with $M_h/M_g = 0.001$ and 0.0003 , lower than the values consid-

ered by Merritt & Quinlan. We find in both cases that the predicted evolution times are longer than 10^3 orbital periods. Only the faintest and densest ellipticals have crossing times short enough (equation 18) for such gradual evolution to be interesting. However, such galaxies tend to have steep central density cusps (Gebhardt et al. 1996), and Figure 21a suggest that steep cusps would themselves induce evolution at a higher rate. We conclude that black holes with fractional masses below $\sim 10^{-3}$ are not likely to be important in producing global evolution of their host galaxies.

If we assume that values of $F \approx 0.28$ imply strong evolution toward axisymmetry in our black-hole-free models as well, Figure 21a implies evolution times of $\sim 10^2$ half-mass orbital periods for galaxies with the steepest cusps, $\gamma \approx 2$, increasing rapidly for smaller γ . We conclude that – in the absence of a central black hole – only the steepest cusps are capable of inducing significant evolution in the shapes of triaxial galaxies over their lifetimes.

7 DISCUSSION

Much of the pioneering work on elliptical galaxy dynamics was carried out in the context of integrable potentials (Kuzmin 1956, 1973; de Zeeuw & Lynden-Bell 1985; de Zeeuw 1985). More recent work (Schwarzschild 1993; Merritt & Fridman 1996; Merritt 1997) has emphasized the importance of stochasticity in triaxial models with density profiles that mimic those of real elliptical galaxies. The latter studies have typically relied on diagnostics like surfaces of section or Liapunov exponents to distinguish regular from stochastic orbits. The frequency mapping technique, first implemented in the context of galaxy dynamics by Papaphilippou & Laskar (1996, 1998), represents a significant advance since it allows one to quickly and accurately calculate the rate at which chaos induces changes in the action-angle variables that characterize an orbit. By contrast, Liapunov exponents reveal only the mean rate of divergence in the immediate vicinity of the orbit, a quantity which may be large even if an orbit is confined to a narrow phase-space region over long periods of time. Frequency mapping also allows the structure of phase space to be represented in terms of the quantities that are most important for the dynamics, the ratios between the fundamental frequencies.

The phase space of triaxial stellar systems is enormously complex and our study has revealed only a small part of that complexity. There are many obvious areas for further study. Figure rotation is a common feature of N -body galaxies and there is some evidence that triaxiality is often associated with rapidly-rotating systems like galactic bulges (Kormendy 1982). While there exists a large body of work on the orbital dynamics of rotating barred galaxies (as reviewed by Contopoulos & Grosbøl 1989 and Sellwood & Wilkinson 1993), much less is known about orbits in rotating triaxial systems with steep central density profiles similar to those of galactic bulges. Another fruitful area for investigation is the character of stochastic diffusion. We argued here that diffusion could be modelled as a random walk in frequency space, but this approximation is undoubtedly very crude. One ex-

pects to see qualitatively different types of diffusion depending on the local structure of phase space (Laskar 1993). At one extreme, when stochastic layers from many resonances overlap, the diffusion should be rapid and extensive. At the other extreme, Arnold diffusion along a single resonance line is expected to be extremely slow.

As important as these studies will be for understanding the detailed dynamics of triaxial stellar systems, we believe that it is already possible to draw two, reasonably secure conclusions about real elliptical galaxies.

First, the timescale for stochastic diffusion in triaxial stellar systems is often comparable to or shorter than galaxy lifetimes. Galaxy crossing times vary in a fairly systematic way with luminosity (equation 18); to the extent that elliptical galaxies of all luminosities begin their lives with triaxial shapes, the typical degree of dynamical evolution should therefore be greatest in faint ellipticals which have the shortest crossing times. One consequence should be a preference for more nearly axisymmetric shapes among fainter ellipticals. We argued that, in galaxies containing a “typical” black hole with $M_h/M_g \approx 0.5\%$, the dynamical evolution time is roughly equal to a galaxy lifetime when $M_B \approx -19$. There is in fact some evidence that the shapes of elliptical galaxies undergo a systematic change at about this luminosity and that bright ellipticals are moderately triaxial as a class (Franx, Illingworth & de Zeeuw 1991; Tremblay & Merritt 1996). The steep dependence of radio luminosity on absolute magnitude has also been taken as evidence that bright ellipticals are more triaxial than faint ellipticals (Auremma et al. 1977; Bicknell et al. 1997).

Second, we found that the structure of phase space in triaxial stellar systems undergoes a qualitative change as the degree of central concentration is increased. When the mass of a central singularity exceeds $\sim 2\%$ the mass of the galaxy, a transition to global stochasticity occurs in the phase space of boxlike orbits. One would expect to observe a very rapid evolution in the shape of a triaxial galaxy when this critical mass is exceeded, since in the globally-stochastic regime, boxlike orbits lose their distinguishability in just a few crossing times. Merritt & Quinlan (1998) have in fact verified that an initially triaxial galaxy evolves toward an axisymmetric state in little more than a crossing time when M_h/M_g exceeds $\sim 2.5\%$. Remarkably, real galaxies also seem to know about this critical mass ratio: the distribution of M_h/M_g (with M_g defined as the mass of the bulge in spiral galaxies) appears to fall off sharply above $\sim 2\%$ (Magorrian et al. 1998), and the two galaxies with the largest ratios of black hole mass to bulge mass, NGC 3115 and NGC 4342, both have $M_h/M_g \sim 0.025$ (Kormendy et al. 1996; van den Bosch 1997). Merritt & Quinlan (1998) argue that this agreement is more than a coincidence. The fueling of massive black holes in quasars and AGN requires matter to be funneled into the nucleus from large distances, and a number of lines of evidence suggest that gravitational torques from non-axisymmetric perturbations are a necessary ingredient (Shlosman, Begelman & Frank 1990). A sudden transition to axisymmetry in the stellar distribution would therefore be expected to limit the mass of a central black hole.

We are tempted to incorporate these ideas into a more

complete picture of elliptical galaxy evolution, as follows. We suppose that elliptical galaxies begin their lives as gas-rich disks. The bulges of these disk galaxies contain black holes, which form from gas that is channeled into the nucleus by gravitational torques from the (triaxial) bulge and/or stellar bar. This growth is halted (presumably at the end of the quasar epoch, at $z \approx 2 - 3$) when the black holes have accreted $\sim 2\%$ the mass of their host bulges, at which point the infall of matter comes to a halt as the bulges acquire axisymmetric shapes. Subsequent mergers between disk galaxies convert many of them into ellipticals; the black holes also merge, coming to rest in the nuclei of the merged galaxies. Mergers have two important consequences for the subsequent dynamics. First, they convert gas into stars and disks into spheroids, thus reducing the average value of M_h/M_g below the critical value that generates global stochasticity in the bulge – perhaps to $\sim 0.5\%$, the average value observed in early-type galaxies in the nearby universe. Second, mergers create triaxial systems from initially axisymmetric ones. Taken together, these two facts imply different end states for bright and faint ellipticals. Bright ellipticals, with their low central densities and long crossing times, would tend to retain their (merger-induced) triaxial shapes. Faint ellipticals, with their high central densities and short crossing times, would remain close to axisymmetric. The result, at the present epoch, would be an apparent dichotomy, with bright, triaxial ellipticals at one extreme and faint, axisymmetric ellipticals at the other.

The existence of two families of elliptical galaxies with distinct morphologies has in fact been emphasized by Kormendy & Bender (1996), who argued that elliptical galaxies should be divided into two groups, disky and boxy, based on the deviations of their isophotes from ellipses. We note that strong boxiness is a generic feature of N -body galaxies, whether formed via collapse (Udry 1993), dynamical instabilities (Raha et al. 1991), accretion (Quinn & Goodman 1986), mergers (Hernquist 1990), tidal torquing (May, van Albada & Norman 1985), etc. The ubiquity of boxiness in N -body galaxies is a consequence of the fact that regular orbits, both tubes and boxes, have dimpled shapes when seen in projection. A galaxy constructed from such orbits is likely to be boxy too unless the distribution of orbital turning points is chosen to be sufficiently smooth (Binney & Petrou 1985). The interesting question is: How do some elliptical galaxies *avoid* being very boxy? One plausible answer, suggested by Figure 16, is that stochastic diffusion eliminates sharp features in the turning-point distribution of the boxlike orbits. N -body simulations (Friedli & Benz 1993; Merritt & Quinlan 1998) provide some support for this idea: the growth of a central mass concentration can convert a boxy, triaxial system into an axisymmetric one with accurately elliptical isophotes. We therefore propose that boxiness is an indication that the phase-space distribution has not been strongly influenced by stochastic diffusion. In support of this view, we note Kormendy & Bender's (1996) observation that boxiness correlates well with kinematical measures of triaxiality (Capaccioli & Longo 1994), consistent with our expectation that triaxiality itself can only be maintained in systems that are dynamically unevolved.

Boxy systems constructed primarily from tube orbits – an example is shown in Figure 12 of Sellwood & Merritt (1994) – would not be strongly affected by stochastic diffusion. This fact might explain the persistence of strong boxiness in the bulges of many disk galaxies (Shaw 1987).

It is often argued (e.g. Kormendy 1990; Faber et al. 1997) that many of the systematic differences between bright and faint ellipticals are due to the greater importance of gaseous dissipation in the formation of the latter. We do not disagree with this view but point out that one of the principal effects of dissipation is to accelerate *stellar dynamical* evolution of galaxies by increasing their mean density and central concentration. For instance, N -body simulations of triaxial or barred galaxies containing a dissipative component often show a sudden change in the galaxy's shape, toward axisymmetry, after a small fraction of the gas has accumulated in the center (Udry 1993; Dubinski 1993; Friedli & Benz 1993; Barnes & Hernquist 1996). While sometimes attributed loosely to "dissipation," this rapid evolution in the stellar distribution can only be due to a change in the character of the orbits resulting from the increased central force. In other words, it is an indication that many of the stellar orbits have become chaotic. Of course, dissipation has other effects as well, most importantly an enhancement of rotational support. Our point here is that a trend of increasing dissipation with decreasing luminosity is not inconsistent with the view that faint ellipticals are dynamically more evolved than bright ellipticals as well.

This work was supported by NSF grants AST 93-18617 and AST 96-17088 and by NASA grant NAG 5-2803. I. Jørgensen kindly provided the data on which Figure 20 is based. We thank J. Laskar, R. Nityananda, Y. Papaphilippou, D. Richstone, J. Sellwood and S. Tremaine for useful discussions. H. Kandrup critically reviewed the initial manuscript and his comments led to substantial improvements in the final version.

REFERENCES

- Auriemma, C. G., Perola, G., Ekers, R., Fanti, R., Lari, C., Jaffe, W. & Ulrich, M. 1977, *A&A*, 57, 41
 Barnes, J. E. & Hernquist, L. 1996, *ApJ*, 471, 115
 Bicknell, G. V., Koekemoer, A., Dopita, M. A. & O'Dea, C. P. 1997, in *The Second Stromlo Symposium: The Nature of Elliptical Galaxies*, A.S.P. Conf. Ser. Vol. 116, eds. M. Arnaboldi, G. S. Da Costa & P. Saha (Provo: ASP), 432
 Binney, J. & Kumar, S. 1993, *MNRAS*, 261, 548
 Binney, J. & Petrou, M. 1985, *MNRAS*, 214, 449
 Binney, J. & Spergel, D. 1982, *ApJ*, 252, 308
 Binney, J. & Spergel, D. 1984, *MNRAS*, 206, 159
 Boozer, A. H. 1982, *Phys. Fluids* 25, 520.
 Capaccioli, M. & Longo, G. 1994, *A&A Rev.* 5, 293
 Carollo, C. M. 1993, PhD Thesis, Ludwig-Maximilians Univ.
 Chapman, S., Garrett, B. C. & Miller, W. H. 1976, *J. Chem. Phys.*, 64, 502
 Chirikov, B. V. 1960, *Plasma Physics (J.N.E. Pt. C)* 1, 253
 Contopoulos, G. 1971, *AJ*, 76, 147.
 Contopoulos, G. & Grosbøl, P. 1989, *Astron. Astrophys. Rev.*, 1, 261.

- Dehnen, W. 1993, MNRAS, 265, 250
- de Zeeuw, T. 1985, MNRAS, 216, 273
- de Zeeuw, T. & Lynden-Bell, D. 1985, MNRAS, 215, 713
- Dubinski, J. 1993, ApJ, 431, 617
- Faber, S. M., Dressler, A., Davies, R. L., Burstein, D., Lynden-Bell, D., Terlevich, R. & Wegner, G. 1987, in *Nearly Normal Galaxies*, ed. S. M. Faber (Berlin: Springer), 175
- Faber, S. M., Tremaine, S., Ajhar, E. A., Byun, Y. I., Dressler, A., Gebhardt, K., Grillmair, C. Kormendy, J., Lauer, T. R. & Richstone, D. O. 1997, AJ, 114, 1771
- Ferrarese, L. et al. 1994, AJ, 108, 1598
- Franx, M., Illingworth, G. D. & de Zeeuw, P. T. 1991, ApJ, 383, 112
- Fridman, T. & Merritt, D. 1997, AJ, 114, 1479
- Friedli, D. & Benz, W. 1993, A&A, 268, 65
- Gebhardt, K. et al. 1996, AJ, 112, 105
- Goodman, J. & Schwarzschild, M. 1981, ApJ, 245, 1087
- Habib, S., Kandrup, H. E. & Mahon, M. E. 1997, ApJ, 480, 155
- Hairer, E., Nørsett, S. P. & Wanner, G. 1993, Solving Ordinary Differential Equations I. Nonstiff Problems (Berlin: Springer)
- Hernquist, L. 1990, ApJ, 400, 460
- Hunter, C. 1995, Ann. NY Acad. Sci. 751, 76
- Jørgensen, I., Franx, M. & Kjærgaard, P. 1995, MNRAS, 273, 1097
- Jørgensen, I., Franx, M. & Kjærgaard, P. 1996, MNRAS, 280, 167
- Kaasalainen, M. 1995, MNRAS, 275, 162
- Kaasalainen, M. & Binney, J. 1994, MNRAS, 268, 1033
- Kandrup, H. E., Eckstein, B. L. & Bradley, O. B. 1997, A&A, 320, 65
- Kandrup, H. E. & Mahon, M. E. 1994, Phys. Rev. E, 49, 3735
- Karney, C. F. F. 1983, Physica 8D, 360
- Kormendy, J. 1982, ApJ, 257, 75
- Kormendy, J. 1990, in *Dynamics and Interactions of Galaxies*, ed. R. Wielen (Berlin: Springer), 499
- Kormendy, J. & Bender, R. 1996, ApJ, 464, L119
- Kormendy, J. et al. 1996, ApJ, 459, L57
- Kormendy, J. & Richstone, D. O. 1995, ARA&A, 33, 581
- Kuo-Petravic, G., Boozer, A. H., Rome, J. A. & Fowler, R. H. 1983, J. Comput. Phys., 51, 261
- Kuzmin, G. G. 1956, Astr. Zh., 33, 27
- Kuzmin, G. G. 1973, in *The Dynamics of Galaxies and Star Clusters*, ed. T. B. Omarov (Nauka of the Kazakh S. S. R., Alma-Ata), 71.
- Laskar, J. 1990, Icarus, 88, 266
- Laskar, J., Froeschlé, C. & Celletti, A. 1992, Physica D, 56, 253
- Laskar, J. 1993, Physica D, 67, 257
- Laskar, J. 1996, Introduction to Frequency Map Analysis, in NATO-ASI, Hamiltonian Systems with Three or More Degrees of Freedom, eds. C. Simo & A. Delshams (Dordrecht: Kluwer), in press
- Lichtenberg, A. J. & Leiberman, M. A. 1992, Regular and Chaotic Dynamics (Berlin: Springer)
- Macchetto, F., Marconi, A., Axon, D. J., Capetti, A., Sparks, W. & Crane, P. 1997, ApJ, 489, 579
- Magorrian, J. et al. 1998, CITA Preprint No. CITA-97-28, astro-ph/9708072
- Mahon, M. E., Abernathy, R. A., Bradley, B. O. & Kandrup, H. E. 1995, MNRAS, 275, 443
- May, A., van Albada, T. S. & Norman, C. A. 1985, MNRAS, 214, 131
- McGill, C. A. & Binney, J. 1990, MNRAS, 244, 634
- Merritt, D. 1997, ApJ, 486, 102
- Merritt, D. & Fridman, T. 1995, A. S. P. Conf. Ser. Vol. 86, Fresh Views of Elliptical Galaxies, ed. A. Buzzoni, A. Renzini & A. Serrano (Provo: Astronomical Society of the Pacific), 13
- Merritt, D. & Fridman, T. 1996, ApJ, 460, 136
- Merritt, D. & Quinlan, G. 1998, ApJ, May 10
- Merritt, D. & Valluri, M. 1996, ApJ, 471, 82
- Miralda-Escudé, J. & Schwarzschild, M. 1989, ApJ, 339, 752
- Pahre, M., Djorgovski, G. & de Carvalho, R. 1995, ApJ, 453, L17
- Papaphilippou, Y. & Laskar, J. 1996, A&A, 307, 427
- Papaphilippou, Y. & Laskar, J. 1998, A&A, 329, 451
- Percival, I. C. 1974, J. Phys. A., 7, 794
- Prince, P. J. & Dormand, J. R. 1981, J. Comp. Appl. Math.7, 67
- Quinn, P. J. & Goodman, J. 1986, ApJ, 309, 472
- Raha, N., Sellwood, J. A., James, R. A. & Kahn, F. D. 1991, Nature, 352, 411
- Ratcliff, S. J., Chang, K. M. and Schwarzschild, M. 1984, ApJ, 279, 610
- Schwarzschild, M. 1979, ApJ, 232, 236
- Schwarzschild, M. 1993, ApJ, 409, 563
- Sellwood, J. A. & Merritt, D. 1994, ApJ, 425, 530
- Sellwood, J. A. & Wilkinson, A. 1993, Rep. Prog. Phys., 56, 173
- Shaw, M. A. 1987, MNRAS, 229, 691
- Shlosman, I., Begelman, M. C. & Frank, J. 1990, Nature, 345, 679
- Statler, T. 1987, ApJ, 321, 113
- Tremaine, S. et al. 1994, AJ, 107, 634
- Tremblay, B. & Merritt, D. 1995, AJ, 110, 1039
- Tremblay, B. & Merritt, D. 1996, AJ, 111, 2243
- Udry, S. 1993, A&A, 268, 35
- van den Bosch, F. C. 1997, PhD Thesis, Leiden University
- van der Marel, R. P., de Zeeuw, P. T., Rix, H. W. & Quinlan, G. D. 1997, Nature, 385, 610
- Warnock, R. L. 1991, Phys. Rev. D, 66, 1803